Maximizing the habitat restoration potential of controlled releases at hydropower dams; Understanding impacts of hydrograph form on sediment transport

Megan K Kenworthy

The University of Idaho

2018

1.0. Introduction

Regulation of streamflow for hydropower often alters natural hydrographs, commonly reducing peak flows, increasing baseflows, and increasing ramping rates. Simultaneously, reservoirs typically trap sediment, reducing the supply to the reach downstream of the dam. These changes to the flow regime and sediment supply impact channel morphology and sediment transport processes in ways that reduce the diversity and suitability of instream habitat. A variety of restoration approaches have attempted to mitigate for some of these changes and a growing number include releases of high flows designed to mimic key characteristics of the pre-regulation hydrograph. One example is the Trinity River, CA, where the addition of augmentation gravel to the channel has been combined with high flows designed to restore portions of the pre-regulation hydrograph to improve channel conditions for spawning fish on the Trinity River, CA. Another example is the high-flow experiments on the Colorado River through the Grand Canyon that aim to restore eroding sand bars that not only provide habitat but camping for rafting groups. More projects that restore portions of the pre-regulation hydrograph are likely in the future because the Federal Energy Regulatory Commission (FERC) requires habitat mitigation efforts in the relicensing process for hydropower facilities. However, the outcomes of these costly restoration efforts are often hard to predict because little is known about how hydrograph form actually impacts channel morphology and bedload transport in rivers.

Here we summarize the results of two flume experiments designed to investigate the impacts of hydrograph form on the morphology of a channel bar and bedload transport processes. The first experiment primarily investigated the impacts of hydrograph recession rate on the morphology of a channel-bar in a sand bed channel. Additional runs examined the combined effects of hydrograph recession and a dense patch of vegetation on bar form. The second flume experiment investigated bedload transport processes in an armored, gravel bed channel during hydrographs with varying form. It documented total bedload flux for a hydrograph, bedload flux rates, persistence of the coarse armor surface, and changes in bed surface structure. Both experiments observed

links between hydrograph form and the resulting bar morphology or bedload transport processes, providing insight into ways that high flow hydrographs can be designed to better facilitate restoration goals downstream of hydropower facilities.

2.0. Impacts of hydrograph recession rate and vegetation on bar morphology in a sand bed channel

2.1. Introduction

Nearly all natural channels are subject to unsteady flows, and there is considerable variability among hydrographs of different hydrologic regimes, from gradually changing (snowmelt or groundwater driven) to "flashy" events with rapidly changing discharges (rain dominated). Regulation of many stream channels across the globe has altered natural hydrographs (Dynesius & Nilsson, 1994) to better serve the needs of irrigation, flood control, or hydropower. In addition, climate change already has, or is predicted to alter the flow regimes of many streams (Clark, 2010; Hamlet & Lettenmaier, 2007; Luce & Holden, 2009; Schnorbus et al., 2014). Areas in the rain-snow transition are especially at risk of shifting from snow to rain dominated hydrographs. On regulated rivers, climate change is also driving changes to the regulated hydrographs (Lake et al., 2012; Yao & Georgakakos, 2001). Despite the prevalence of unsteady flows, large gaps remain in understanding how hydrographs form influences channel morphology.

One indication that hydrograph form is an important driver of morphology is channel response following flow regulation. Diversions that reduce flow and transport capacity have been linked to significant instream aggradation (Wesche et al., 1988), and fining of the bed grain size distributions (Baker et al., 2011). Dam operations can vary based on the main function of the facility, but frequently, base flows are artificially high, peak flows reduced, and ramping rates faster than pre-regulation (Kondolf, 1997; Magilligan & Nislow, 2005; Poff et al., 2007; Singer, 2007). Simultaneously, sediment supply is typically reduced by impoundment within the reservoir. The resulting downstream channel responses can include coarsening of the bed grain size distribution (Dominick & O'Neill, 1998); channel entrenchment and abandonment of the former floodplains (Church, 1995; Petts & Gurnell, 2005) or, conversely, channel aggradation (Petts & Gurnell, 2005); vegetation encroachment (Church, 1995; Dominick & O'Neill, 1998; Gordon & Meentemeyer, 2006); and a reduction in overall geomorphic complexity (Gordon & Meentemeyer, 2006). However, separating the sole influence of the

hydrograph from simultaneous reductions in sediment supply or changes in land use adjacent to a channel can be very difficult in field settings.

Recent experimental (Humphries et al., 2012; Lee et al., 2004; Mao, 2012; Martin & Jerolmack, 2013; Waters & Curran, 2015) and modeling (Ghimire & Deng, 2013; C. B. Phillips et al., 2013; Shen & Diplas, 2010; Viparelli et al., 2011) investigations also point to the influence of unsteady flow on channel characteristics. One way this may occur is through the total sediment transported by an unsteady flow. Some studies have documented a decrease in total sediment flux compared to an equivalent steady flow (Bell & Sutherland, 1983; Griffiths, 1976; Young & Davies, 1991), while other have documented an increase (Bombar et al., 2011; Lee et al., 2004), or no change at all (Gary Parker et al., 2007). The variability in findings may result in part from differences in hydrograph form because "flashier" hydrographs have been linked to greater total bedload flux than an equivalent but more gradually changing hydrograph (Yen & Lee, 1995). There is evidence that hydrograph form influences additional channel characteristics. More gradual hydrographs have been linked to enhanced vertical sorting (i.e. armor development; Hassan et al., 2006) but decreased transverse sorting around a bend (Yen and Lee, 1995) compared to "flashier" events. The formation, size and spacing of beforms also respond to hydrograph form (Martin & Jerolmack, 2013; Waters & Curran, 2015).

This study investigated how varying falling limb recession rate influenced the morphology of a forced bar in a sand bed channel. This work was motivated by understanding how changes to the gradual recession of snowmelt driven hydrographs might alter bar morphology. Many species in snowmelt dominated systems time key life stages to coincide with the annual snowmelt recession (e.g. vegetation recruitment, migration, reproduction). For example, cottonwood seeds disperse during the spring recession, which allows seeds to germinate on fresh bar deposits, after which root growth keeps pace with the gradual drop of the water table (Braatne et al., 2007; Cooper et al., 1999; Rood et al., 1995). This key feature of snowmelt driven hydrograph is often lost or significantly truncated by regulation. Increasingly, habitat mitigation for hydroelectric facilities includes restoration of the gradual spring recession. One example is the high flow experiments on the Colorado River through the Grand Canyon where a key goal is rebuilding the diminished sand bars (refs). Projects like this

need more information about the influence of hydrograph form to design high flows that best aid restoration goals.

2.2. Methods

2.2.1. Flume experiments

Hydrograph experiments were run at the Saint Anthony Falls Laboratory's Outdoor Stream Lab (OSL) in Minneapolis, MN. This unique facility combines a meandering channel and vegetated floodplain with control over channel discharge and sediment feed rates (Figure 1). Further, though the bank positions and two riffles are fixed into position, the morphology of the rest of the channel bed (predominantly in the coarse sand range with a D_{50} of 0.7 mm) is free to respond to imposed discharges, feed rates, or other experimental treatments. Total channel length is 40 m with an average bankfull width of 2 m and slope of 0.007 (Rominger et al., 2010).

The focus of the study was the morphology of the forced bar that forms on the middle meander (Figure 1). An instrument cart was set up over the bar apex to obtain detailed measurements before, during and after experiments. Before and after runs, topography of exposed portions of the bar were measured with a Keyence laser scanner (1x1 cm resolution). During experiments, submerged portions of the bar were measured using a sonar scanner (1x5 cm resolution). Fifteen cross-sections were also installed throughout the channel where we measured bed elevation by point-gage in 10 cm intervals and water surface elevation in at least three locations. A total station to survey of the cart and cross-section positions allowed all topography to be put into a single local coordinate system.

Each of three recession runs was preceded by an equilibrium run (EQ; Table 1) to establish similar starting conditions for experiments. Discharge and sediment feed rates were held constant (112 L/s and 2.14 kg/min). The equilibrium discharge fully submerged the bar, allowing the movement of sediment across the top. The feed rate equaled the transport capacity as estimated by a modified Meyer-Peter-Mueller equation that was calibrated using the mean flux rate for bankfull flow. EQ runs continued until equilibrium was established in the channel, denoted by stabilization of bar morphology and bed elevations throughout the channel. To determine

when equilibrium had been reached, we measured bed elevations at regular intervals in all cross-sections and marked the downstream extent of bar growth with pin flags.

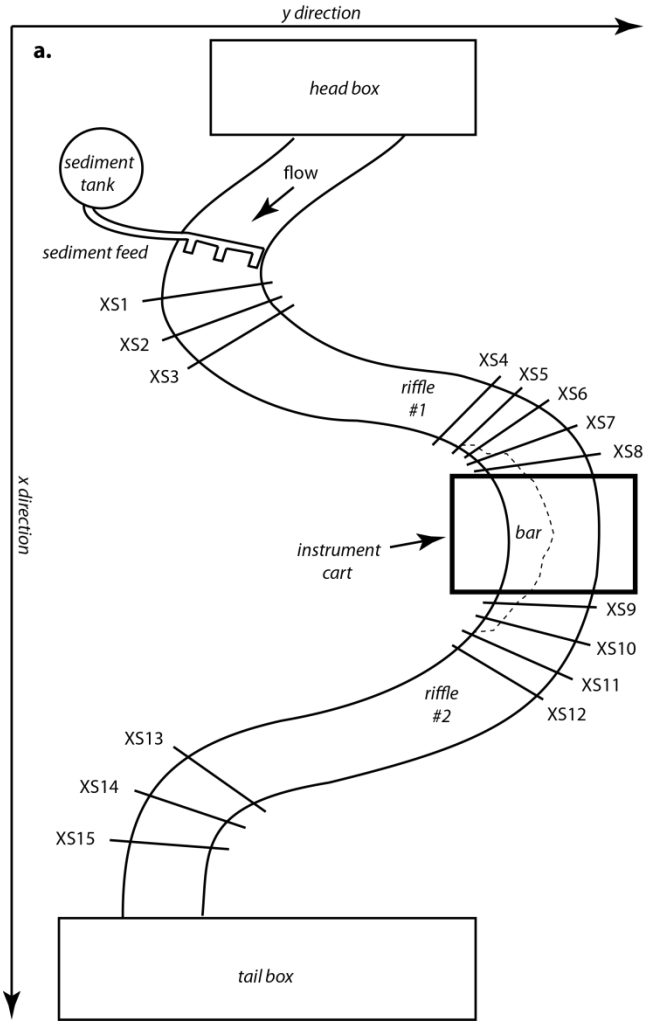

Figure 1. Layout of the St. Anthony Falls Outdoor Streamlab and experimental setup.

Table 1. Recession hydrograph characteristics.

hydrograph	*min Q (L/s)*	*max Q (L/s)*	*duration (hrs)*	*recession rate*[a] *(%)*	*total water volume (m^3)*	*total sediment input (kg)*
EQ	112	112	11-25	na	variable	variable
H10, H10V	72	150	8	10	3075	962
H30, H30V	68	284	5	30	2835	1014
H60	71	284	6	61.5	2852	971

a. For runs H10, H10V, H30, and H30V recession rate is the decrease in discharge at every time-step. For H60, the recession rate is the maximum change in discharge as the recession rate was variable through the run.

Hydrograph runs were limited to the falling limb only (Figure 2). Total transport capacity (estimated assuming steady-state flow), total volume of water, and total sediment feed were kept as close as possible among runs (± 10%; Table 1). Run durations were determined by the amount of time required to transport an estimated quantity of sediment capable of resulting in significant morphological change on the bar. Minimum discharge (68-72 L/s) produced little sediment transport over the bar while peak flows (284 L/s and 150 L/s) fully submerged the bar top. Recession hydrographs were step-wise with time-steps of one hour (Figure 2). Runs were designed to simulate snowmelt dominated (H10), rain dominated (H30), and regulated (H60) recession hydrographs. Rather than use a constant sediment feed rate it was adjusted at each time-step to equal the estimated transport capacity. This helped isolate the influence of recession hydrographs by minimizing any impacts from a changing ratio of sediment supply to transport capacity.

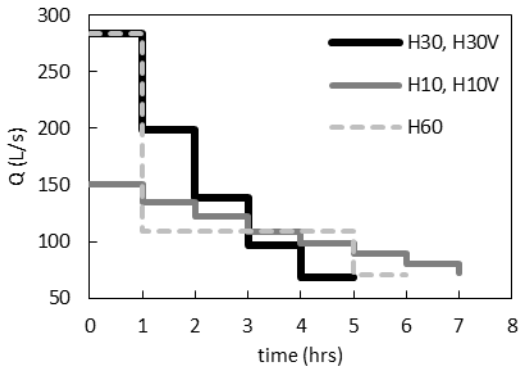

Figure 2. Recession limb hydrographs with corresponding sediment feed rates, which were held equal to the estimated transport capacity throughout each run.

The H10 and H30 hydrograph were repeated with vegetation installed on the bar-top (H10V and H30V). Once equilibrium was established, plugs of *juncus effusus* and *carax* were installed in a dense patch on the upstream half of the bar along the bar edge (Figure 3), secured with lengths of metal wire. Patch placement simulated vegetation establishment along a line of elevation. The more rigid *juncus* approximated an older patch established at the head of the bar, while the less rigid *carax* approximated younger plants at a lower position on

the bar-top. The *juncus effuses* plants had a mean stem height of 21.1 cm and frontal width of 3.4 cm, while the *carax* had an average height of 9.5 cm and width of 4.6 cm. The total area of the vegetation patch was approximately 0.62 m^2. After the vegetation was in place the bar top was scanned by laser and the total station used to survey the perimeter of the vegetation patch.

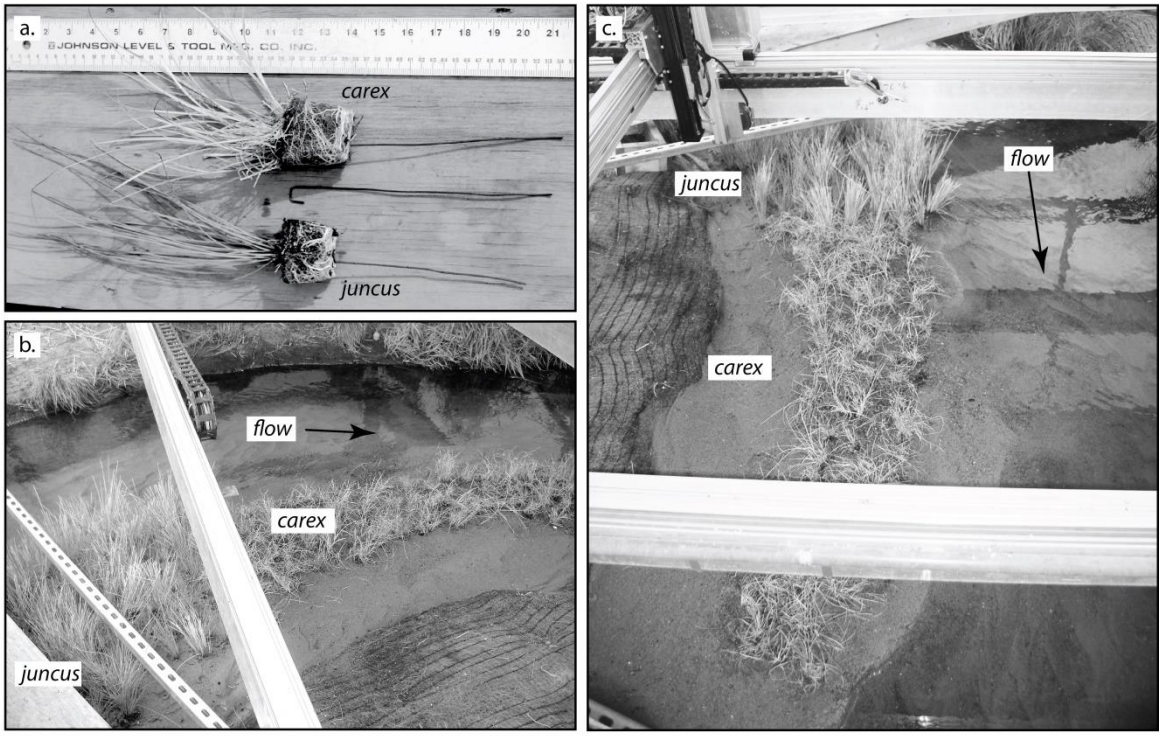

Figure 3. a) Vegetation plugs with wired used to install the vegetation patch during the H10V and H30V runs. Images in b) and c) provide views of the patch installed on the bar.

2.2.2. Quantifying bar morphology

Topography of the bar and the adjacent pool for a given time-step was obtained by combining the point cloud data of laser scans, sonar scans, and cross-sections. Sonar scans during runs were the average of eight consecutive passes, which largely removed the influence of migrating ripples. A surface was fit to the combined data then edited by hand to remove outliers and unrealistic topographic features. Coordinates were then exported from the resulting surface on a range of grid sizes, the smallest 2x2 cm. Most analysis of the topography used the more detailed 2x2 cm grid only but analysis of differences in the elevation distributions used a range of grid sizes.

Before measuring components of bar morphology (i.e. width and area), we had to objectively identify the break between the bar-top and side, or bar edge. We hypothesized that as the elevation of an artificial water surface increased, there would be a rapid increase in the area submerged upon reaching the relatively flat bar-top. We identified this elevation by estimating the first derivative of the elevation-area inundated relationship with a moving window (Figure 4). Once we identified bar-edge elevation we highlighted all points at that elevation on the bar topography. We removed points that were obviously disconnected from the line defining the bar edge. Using the known position of the channel edge we could then extract the bar-top.

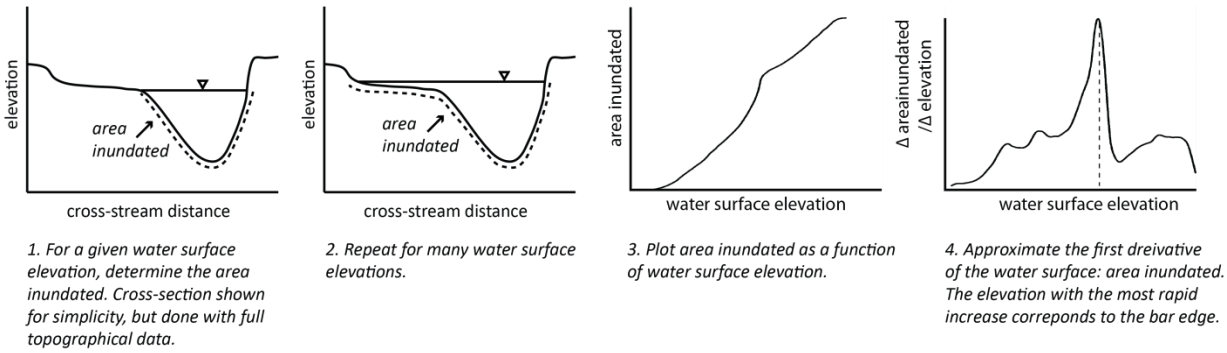

Figure 4. Bar edge was identified using the change in area inundated with changes in water surface elevation, and used the full topography rather than cross-sections. The elevation of the bar edge was located where the most rapid increase in area inundated occurred for set small change in elevation.

Once bar-tops were identified, we could measure and compare the elevation of the bar edge, bar-top area, mean bar-top width, bar-top length, and estimated volumes of scour and deposition among runs. Net volumetric scour and deposition for time-periods of interest were estimated by subtracting initial from final topographies. Elevation distributions were compared for the bar-pool, bar-top only, and pool areas. We first removed portions of the bank with fixed elevation then used the non-parametric, rank-based Kruskal-Wallis test to test for significant differences. When a significant difference was indicated ($p < 0.05$), we used Dunn's multiple comparison test to determine which distributions were significantly different. We repeated the analysis for a range of grid sizes, from 2x2 cm to 40x40 cm. The more dissimilar two distributions were, the larger the grid size would have to be for

them to become statistically indistinguishable. Conversely, more similar distributions would become indistinguishable at smaller grid spacing.

2.3. Results

2.3.1. Equilibrium runs

Qualitatively, the EQ bars were all visually similar with well-defined, broad, flat tops (Figure 5a). The mean width and length were all very similar for the equilibrium bars (Figure 6), but bar-top area and edge elevation indicate that the EQ1 bar formed approximately 3-4 cm lower and had a slightly smaller bar-top area compared to the other equilibrium bars. Empirical cumulative probability plots (4 cm grid spacing) also highlight the similarity of equilibrium topography, with the most significant difference again for the EQ1 bar-top which formed slightly lower (Figure 7a-c). For the full scan area, normalized elevation distributions became statistically indistinguishable at a grid-spacing of only 4 cm, suggesting that overall channel form was very similar. However, bar-tops and non-bar regions became statistically indistinguishable at larger grid sizes of 12 and 14 cm, respectively, suggesting larger differences in elevation distributions for specific regions.

2.3.2. Recession hydrographs without vegetation

Measurements of final bar-top areas, mean widths, and lengths show that H10 increased bar-top size, while H30 and H60 decreased bar-top size compared to the initial bars (Figures 5 and 6). In addition, the H10 bar-edge formed at a lower elevation than the H30 and H60 edges (Figure 6c). As a result, the H10 bar-top had more typical morphology with a broad, well-defined flat top, while the H30 and H60 bar-tops were more irregular and poorly defined. In addition, all three runs increased bar-edge elevation; (Figure 6c and Table2). Cross-sections (Figure 8) also highlight differences in the final bar morphologies. At the upstream end (Figure 8a), the H10 bar-top was lower than H30 and H60. Mid-bar the distinct, flat top of the H10 bar contrasts with the higher, less distinct bar-tops from H30 and H60 (Figure 8). At the downstream end of the bar (Figure 7d), the H10 bar was higher than H30 and H60 along the inner bank, most likely because these bars did not extend that far downstream. However, there was more deposition near the thalweg during H30 and H60 than H10. In the last cross-section, number 10, (Figure 7e), the difference in topography among these three runs is largely diminished.

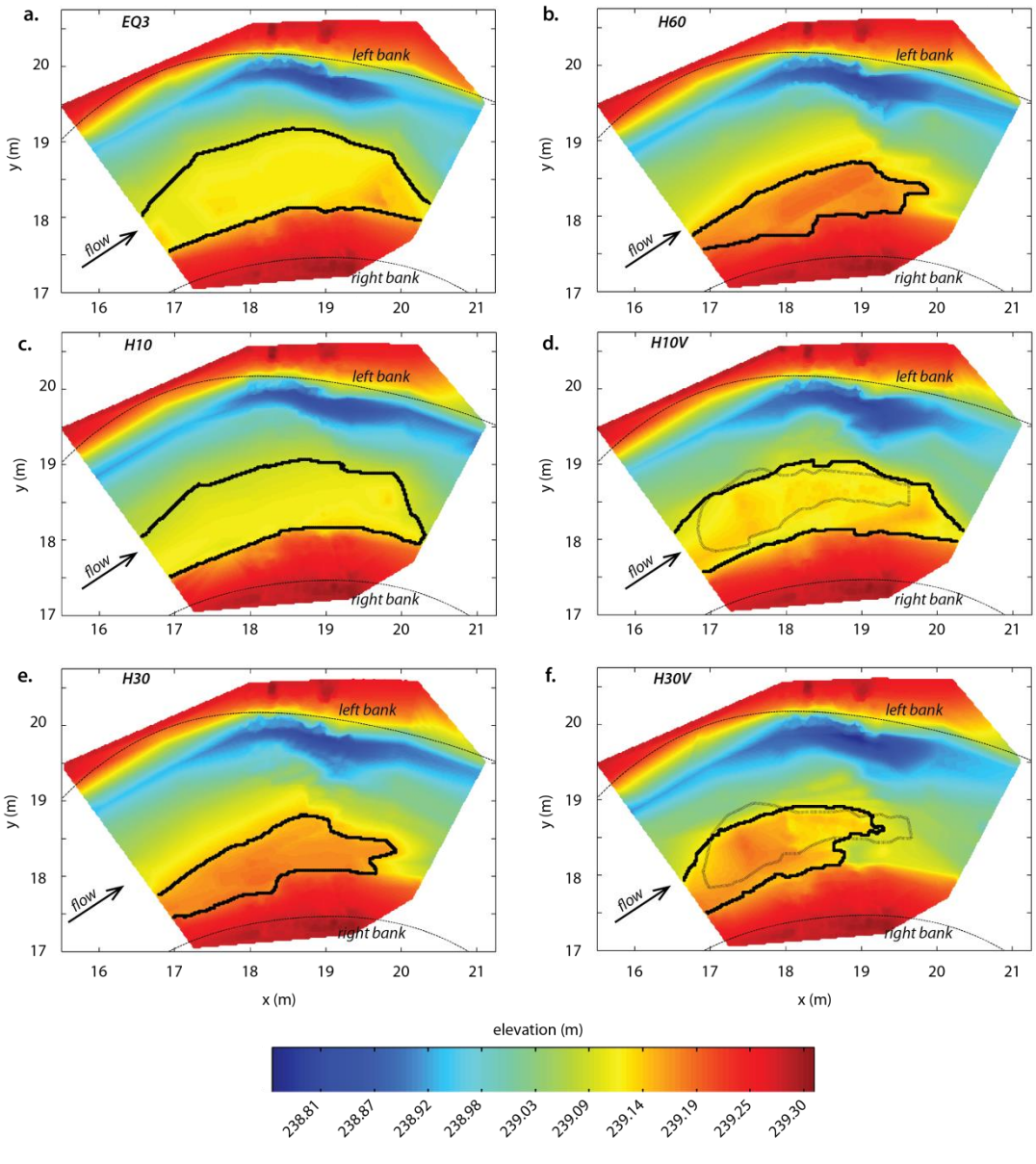

Figure 5. Final bar morphologies from experimental runs with the bar-top outlined (solid black line). An example of the final morphology from equilibrium runs is shown in (a) for the EQ3 run. The outline of the vegetation patch (dashed black line) installed on the bar-top before runs H10V and H30V is also shown in (d) and (f).

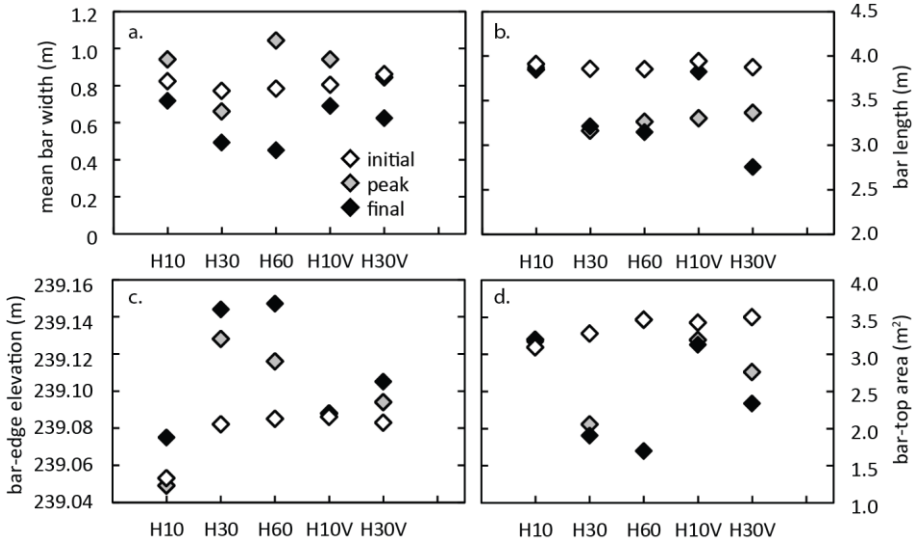

Figure 6. a) Mean bar width, b) bar length, c) bar edge elevation, and d) bar-top area for starting, peak, and final bars. H60 peak flow bar-top area is not visible because it is the same as the initial area.

Table 2.

Run	*initial bar-edge elevation (m)*	*peak bar-edge elevation (m)*	*final bar-edge elevation (m)*	*initial bar-top area (m^2)*	*peak bar-top area (m^2)*	*final bar-top area (m^2)*	*initial bar width (m)*	*peak bar width (m)*	*final bar width (m)*	*initial bar length (m)*	*peak bar length (m)*	*final bar length (m)*	*volume change at peak (m^3)*	*volume change after peak (m^3)*	*total volume change (m^3)*
H10	239.05	239.05	239.08	3.09	3.20	3.17	0.82	0.94	0.72	3.91	3.85	3.87	0.04	0.08	0.11
H30	239.08	239.13	239.14	3.28	2.06	1.91	0.77	0.66	0.49	3.86	3.16	3.21	0.05	-0.01	0.04
H60	239.09	239.12	239.15	3.47	3.47	1.70	0.78	1.04	0.45	3.85	3.26	3.15	0.08	-0.05	0.03
H10V	239.09	239.09	239.09	3.43	3.20	3.13	0.80	0.94	0.69	3.94	3.30	3.82	-0.05	-0.03	-0.08
H30V	239.08	239.094	239.11	3.50	2.76	2.34	0.86	0.84	0.62	3.87	3.36	2.76	0.02	-0.09	-0.07

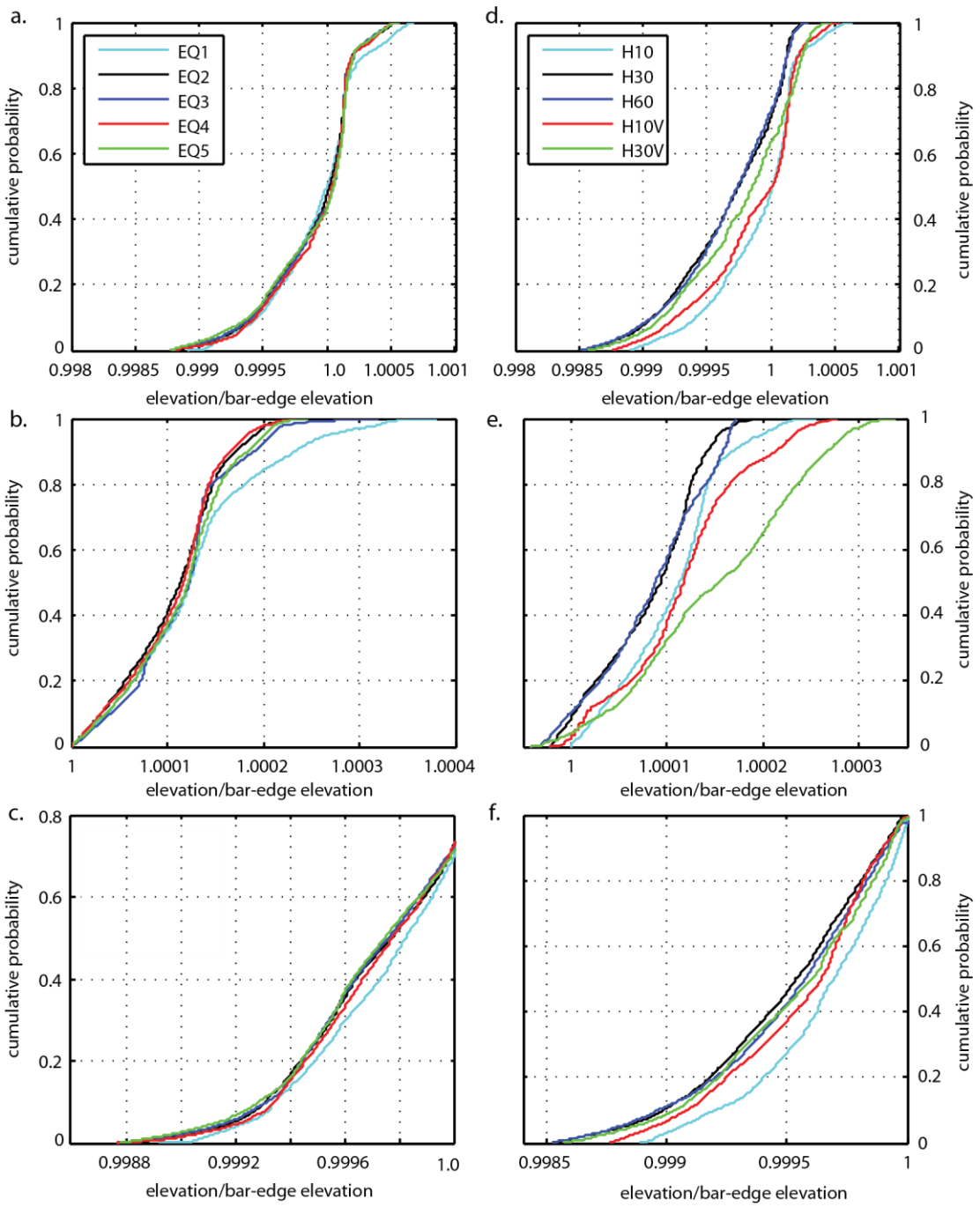

Figure 7. Empirical cumulative probability functions for elevation distributions, normalized by bar-edge elevation. (a-c) shows EQ runs and (d-f) shows the recession hydrographs. The top row shows the full elevation distribution of the bar-pool, the middle row shows bar-top only, and the bottom row shows the non-bar-top region. Plots for the non-bar-top region are limited to elevation at or below the bar-edge.

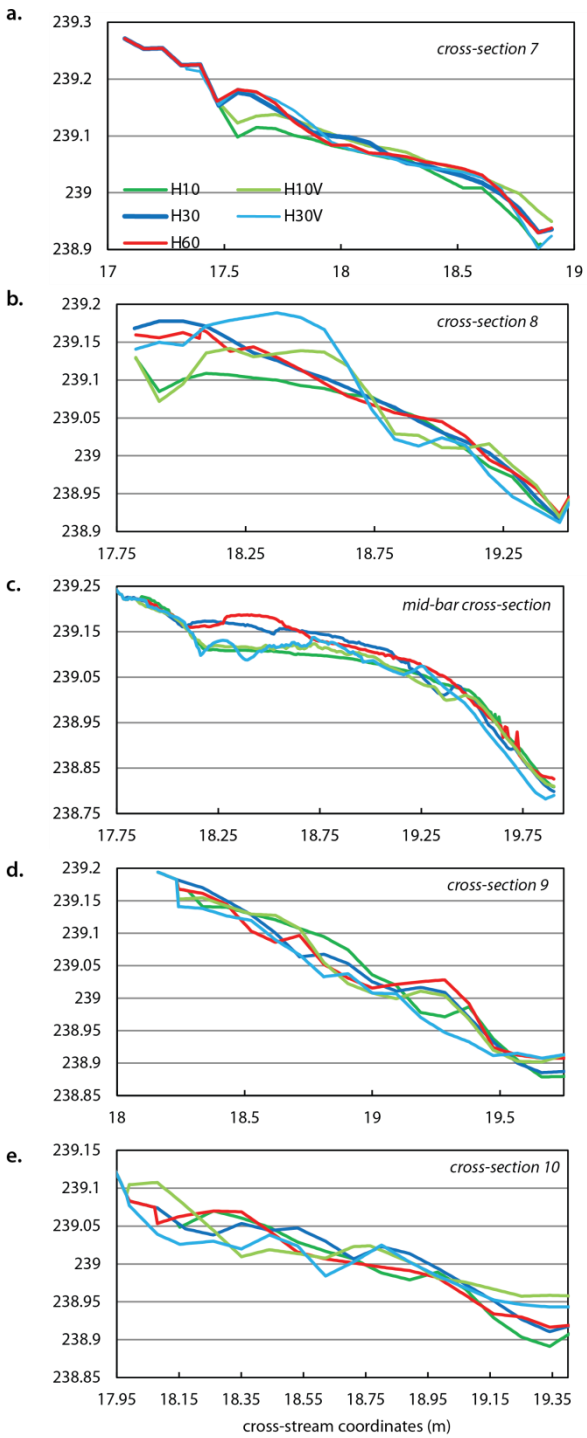

Figure 8. Final cross-sections for all recession hydrographs. Cross-sections are shown from upstream to downstream portions of the bar.

Normalized elevation distributions for the recession runs showed greater variability compared to the EQ runs (Figure 7d-f). For the full bar-pool, H10 is distinct from H30 and H60 at even the smallest grid spacing of 2x2 cm. H30 and H60 did not become statistically different until a very large grid spacing of 36x36 cm, suggesting they were very similar. The results were similar when comparing the bar-top only, with H30 and H60 indistinguishable at a 2 cm grid size, and all three bars indistinguishable with a 16 cm grid size. For the non-bar area, H30 and H60 were distinct up to a 4 cm grid size, and the three became indistinguishable at 28 cm. This indicates that the topography resulting from H10 differs significantly from H30 and H60, but that H30 and H60 resulted in very similar bars.

The magnitude and location of scour and deposition also varied among the H10, H30, and H60 runs. All three resulted in net deposition, estimated as 0.113 m^3 for H10, 0.044 m^3 for H30, and 0.033 m^3 for H60 (Figure 9). However, the spatial distribution of scour and deposition differed (Figure 10b-d). H10 produced fairly uniform deposition over the bar and the thalweg (Figure 10b). In contrast, deposition during H30 and H60 (Figures 10c-d) was primarily on the bar-tops while the thalweg scoured, especially adjacent to the downstream end of the bar. The area of net deposition appears slightly larger for H30 than H60.

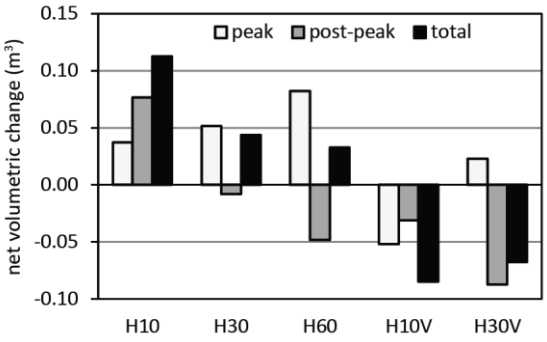

Figure 9. Net volumetric change in sediment for peak flow, all time-steps after peak flow, and full recession hydrographs.

2.3.3. Recession hydrographs with vegetation

H10V and H30V both produced bars with flat, distinct tops (Figures 5 and 8), most similar to H10. The H30V bar-top was more irregular in shape though, and slightly smaller than the H10V bar-top (Figure 5). Both of these runs resulted in decreases in the bar-top area compared to the starting areas (Figure 6d), though the decrease was much larger for the H30V run. The H10V bar-top was only slightly smaller than H10, while the final area for H30V was larger than H30 (Figure 6d, Table 2). Bar-edge elevation remained largely unchanged during H10V (Figure 6a) but increased during H30V.

Significant deposition within the vegetation patch is visible in cross-sections over the bar, particularly cross-section 8 (Figure 8). Just down the bar this deposit was no longer present, and the H10V and H30V bar-tops actually sat lower than those from H10 and H30. Also visible in cross-sections (primarily those of Figure 8a and 8b) was a chute-cutoff channel that formed on the bar-top on the inside of the bend during both of these runs (Figure 11). The chute was quickly scoured at peak flow during H10V, then mostly refilled during the remainder the run. In H30V, the chute scoured in the time-step after peak, then only partially refilled by the end.

Normalized elevation distributions indicate that the vegetation patch produced distinct topography. The H10V topography differed most from H10 at elevations below the bar edge, which were generally higher than H10. H30V resulted in more of the topography distributed above the bar-edge compared to H30. In addition, both were significantly different from all other runs using the finest grid size of 2x2 cm. The vegetation patch also reduced bar-top elevations compared to runs without the patch (Figure 7e). The normalized elevation distribution of the bar-tops only for H10V and H30V were significantly different from all other runs but not each other at the 2x2 cm grid spacing.

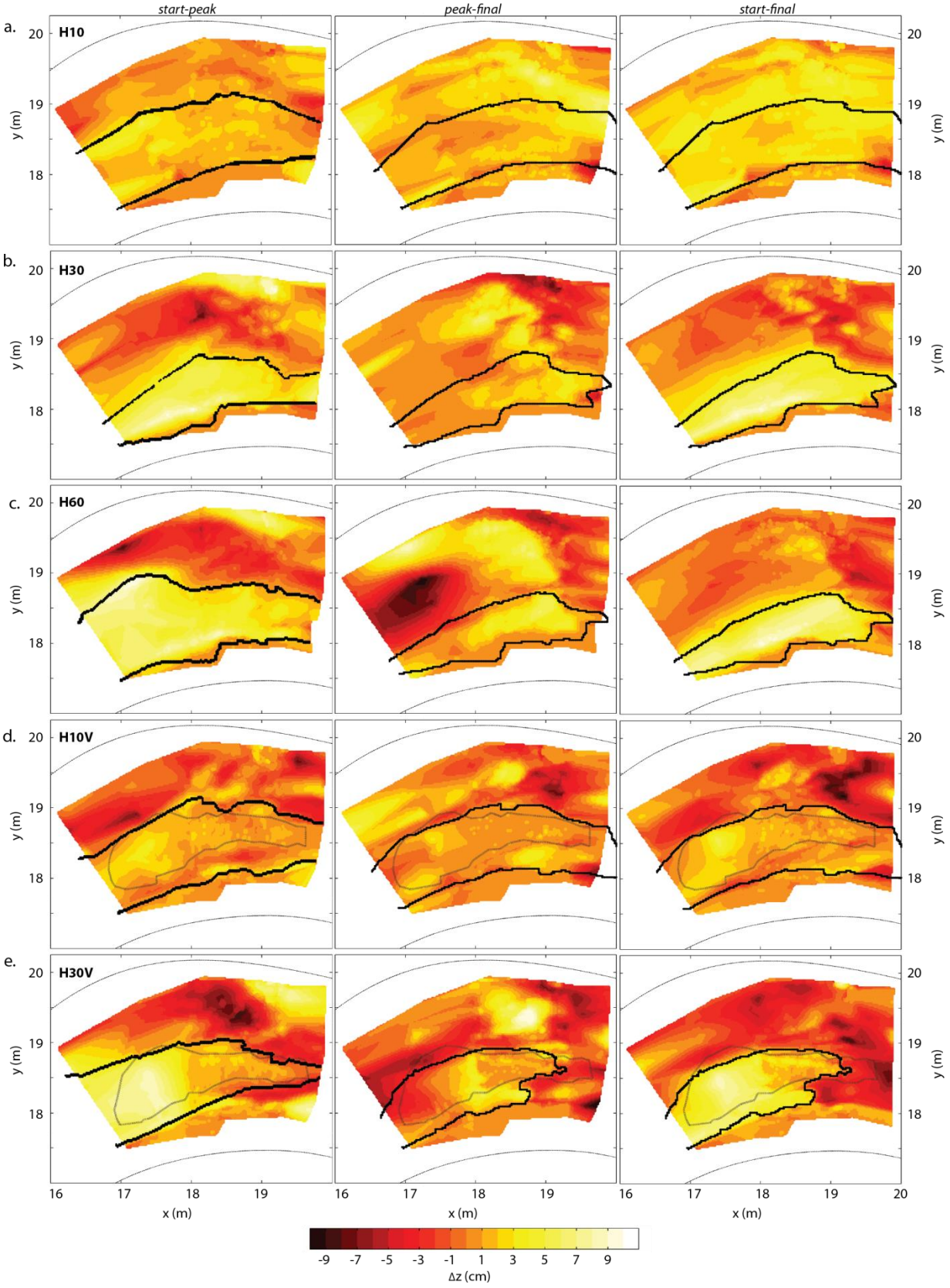
start-peak
peak-final
start-final
a.
H10
b.
H30
c.
H60
d.
H10V
e.
H30V
y (m)
x (m)
Δz (cm)
-9 -7 -5 -3 -1 1 3 5 7 9

Figure 10. (Previous page) Changes in elevation during each recession experiment. The solid black line shows the outline of the bar-top, and the lighter line shows the outline of vegetation patches. The left column shows the elevation changes from start to the end of peak flow, with the peak flow bar-top outlined. The middle column shows changes in elevation from the end of peak to the end of the experiment, with the final bar-top outlined. The right column shows changes in elevation from start to finish, with the final bar-top outlined.

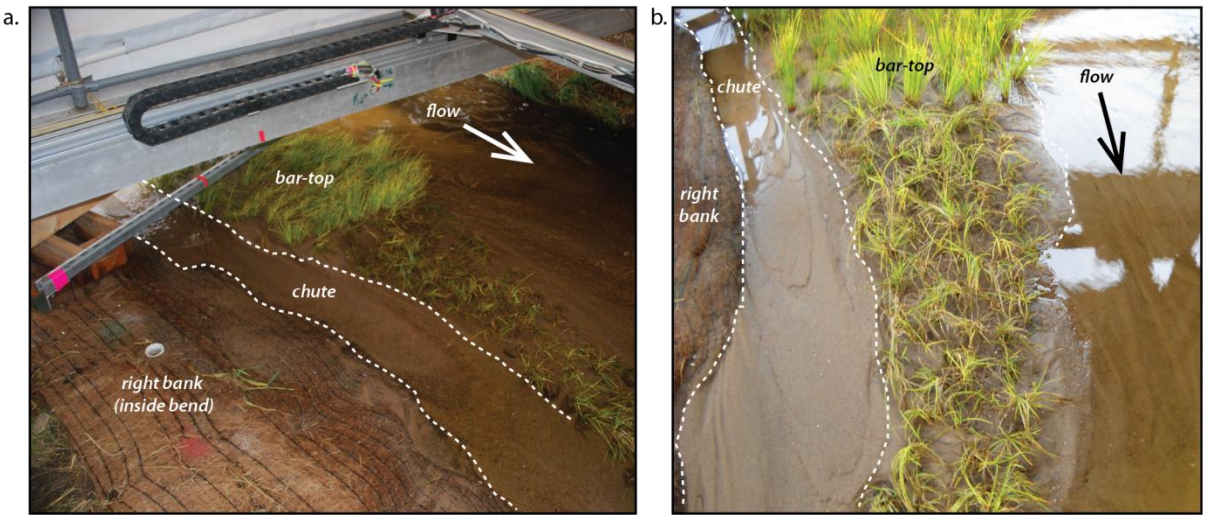

Figure 11. Chute cutoff channel that formed only in runs H10V and H30V. Examples of chute location and remnants at end of H30V (a) and H10V (b).

In contrast to recessions without the vegetation patch, H10V and H30V resulted in net scour (Table2; Figure 9). During H10V, scour occurred primarily adjacent to the bar-top, in the cut-off chute, and in the pool (Figure 10d). Areas of net deposition were limited, with the most significant at the bar head. Net scour during H30V was similar to H10V, but also included much of the downstream end of the initial bar, resulting in a small bar-top area (Figure 10e). However, there was significant deposition within the vegetation patch.

2.3.4 Impacts of peak flow

We also examined bar topography at the end of peak flow in order to compare impacts of the higher peak flow (284 L/s) used in H30, H60, and H30V to the lower peak flow (150 L/s) used in H10 and H10V. Without vegetation, the lower peak resulted in less deposition than the higher peak (Table 2;

Figure 9), and smaller changes to mean bar-top width, length, area, and edge elevation (Figure 6). With vegetation, the lower peak resulted in net scour, while the higher peak resulted in net deposition (Figure 9). For other parameters, results were mixed compared to recessions without vegetation, but overall suggested that the presence of the vegetation patch mitigated the impacts of peak on the bar (Figure 6).

2.4. Discussion

2.4.1. Similarity of initial conditions

Initial conditions provided by equilibrium runs were all very similar with the exception of the first run, in which the EQ1 bar formed at a lower elevation than other equilibrium bars (Figures 6c and 7a). However, normalized elevation distributions were indistinguishable at a 4 cm grid size, suggesting that the EQ1full bar-pool topography was actually quite similar to the other equilibrium runs but shifted lower in the channel. The most likely reason that the EQ1 bar formed lower was conditions of the previous experiment in the facility, which were run at higher discharges and lower sediment feed rates. Like laboratory flumes, the flow and feed rate in the OSL can be controlled, but unlike traditional laboratory flumes, the entire bed of the OSL cannot be replaced or reconfigured between experiments. While this can produce conditions more analogous to the field, it also introduces a greater degree of uncertainty regarding the amount of sediment already on the bed and lasting impacts of previous experiments.

The lower elevation of the EQ1 bar may have impacted results of the H10 run that followed because the resulting bar formed at lower elevation than the H30 and H60 bars (Figure 7). Bar-top area for EQ1 was also slightly smaller than other equilibrium bars (Figure 6d, Table 2), which could have impacted the final size of the H10 bar, though it was significantly larger than those from H30 and H60 anyway. However, the H10V bar also formed lower and had a larger area than the H30V bar (Figures 6 and 7), suggesting this was at least in part a result of the hydrograph used as well.

2.4.2. Differentiating influences of recession rate and peak flow

While we designed hydrographs to best isolate the influence of recession rates, two different peak flow rates were used to maintain the same total transport capacity and volumes of water and sediment (see section 2.1.2.). As a result, the separate impacts of peak and recession rate on resulting bar morphologies must be differentiated as far as possible. The Kruskal-Wallis and Dunn's multiple comparison tests indicated that normalized elevation distributions of the final bar morphologies were significantly different for all runs except the H30 and H60 runs. This could suggest that peak flow was a larger driver of final bar than the hydrograph recession rate. However, while the differences between H30 and H60 are small, the consistent trends in mean bar width, bar length, and bar-top area with recession rate for the runs without vegetation provide evidence that bar-top shrinks as recession rate increases (Figure 6).

A primary influence of peak flow on bar morphology appears to be the amount of deposition on the bar-top during peak. All runs resulted in deposition on the bar-tops at peak, but the higher peak deposited significantly more sediment than the lower peak (Figure 10). Such significant deposition likely had lasting impacts on bar morphology, altering local hydraulics and subsequent locations of scour and deposition. This is supported by previous numerical modeling that demonstrated the significant influence of point bars on local hydraulics, showing that as bars grow larger, the local force balance directs sediment around the head of the bar (Legleiter et al., 2011). The large deposits of the higher peak flow in these experiments may have diverted sediment around the bar for the remainder of the experiment, resulting in the smaller bar-tops of H30, H60, and H30V.

While deposition on the bar-tops at peak appears to have lasting impacts, our observations indicate that recession rates also shaped the final bar. A key way in which this happened was the timing of bar-top emergence. Once the bar-top emerges, deposition on that portion of the bar ceases, and redistribution of that sediment over other portions of the bar becomes very unlikely. During H10 and H10V, the bar remained submerged through the entire recession, allowing continued redistribution and new deposition through the entire run (Figure 10). This may have resulted in part from the smaller

increase in bar elevation due to deposition during peak, but the more gradual recession would have also allowed redistribution of that sand that would have decreased elevation so that the bar-top would not emerge. The recession rates used in H30, H30V, and H60 were too rapid to allow sufficient time for the sediment deposited on the bar-top at peak to be redistributed our scoured enough to prevent the bar-top from emerging. The bar emerged immediately after peak during H60, and at the start of time-step four (3 hrs into the run) during H30 and H30V. Once the bar-tops emerged, continued redistribution of sediment on the bar was minimized, and new deposition on the bar-top impossible. Further, the scour after peak in the thalweg and along the bar edge (Figure 10) could have been driven by emergence of the bar-tops by reducing cross-sectional area and increasing mean velocity. To test this idea, we estimated the mean velocity in cross-section for time-step four of runs H10, H30, and H60. During this time-step the bar-tops of H30 and H60 were no longer submerged, and the discharges were very similar for all runs, 97-109 L/s (Figure 2). H10 had the largest cross-sectional area of 0.29 m^2. For H30 and H60, area was less, 0.22 m^2, due to the higher elevation bar-top that was no longer submerged. The result was lower mean velocity for H10 (0.38 m/s) and H30 and H60 (0.44 and 0.49 m/s, respectively). While these estimates do not give the full picture of shear stress on a smaller scale, they still suggest that emergence of bar-tops due to rapid recession rates can increase mean velocities and erosion, reducing final bar size.

There is limited previous work investigating the influence of hydrograph form on bar morphology, but what is available also suggests that hydrographs do impact bar morphology. An earlier flume experiment by Yen and Lee (1995) investigated the response of a bar formed in a 180° bend to hydrographs with different ramping rates and peak flows. Using full hydrographs instead of only recession limbs, they noted that faster ramping rates deposited sediment at higher elevations on the bar-top, and scour was increased along the outer bank. This is similar to our findings that the faster recession runs of H30 and H60 deposited more sediment on the bar-top. However, Yen and Lee (1995) also varied peak flow, and the hydrographs with faster ramping rates also had higher peak flows. As a result, it is likely that their observations are the result of both peak flows and ramping. Field observations by Hassan

(2005) provide further evidence that flashy regimes produce bars that are more poorly developed than those typically subject to gradually changing flows.

2.4.3. Influence of vegetation patch

The main influence of the vegetation patch appears to have been to drive net scour, rather than net deposition as seen in all other runs without vegetation. There was significant deposition within the vegetation patch itself, but scour elsewhere was enhanced, particularly in the thalweg adjacent to the downstream end of the bar (Figure 10). A previous study in the Streamlab installed vegetation on the same bar and ran a series of steady, bankfull flows to document changes in flow structure and bar form (Rominger et al., 2010). Though the location and density of the plants differed from this study, they also documented deposition in the patch, but scour of the outer edge that decreased bar width. This was attributed to lower velocities within the vegetation patch but increased velocities out of the patch. Though we did not measure velocity during this experiment, it is very likely that the vegetation patch induced similar changes in velocity compared to the runs without vegetation, driving the changes in deposition and scour we documented. Waters and Crowe Curran, (2016) also found that vegetation patches subject to unsteady flow generally reduced reach scale bed stability in flume experiments, indicated by net sediment loss. Only a small range of flow conditions induced reach scale stability with the vegetation.

It is possible that different plants in a different arrangement could have altered the results because many factors determine the impact that vegetation has on sedimentation, channel stability and morphology. For example, plants with greater crown area can induce more sedimentation (Kui et al., 2014). Further, younger, smaller plants have been found to provide less bank stabilization and dampening of flood impacts compared to older, larger plants (Wilcox and Shafroth, 2013). The distribution of plants can also impact bank stability, with more uniform distribution slowing bank retreat and promoting stability of a single-thread channel but non-uniform distribution promoting stable islands and a more braided channel form (Dijk et al., 2013).

2.4.3. Implications for restoration

The differences in final bar morphologies for the recession hydrographs suggest that the design of high flows can be adjusted to enhance restoration goals in sand bed channels. While there are numerous additional considerations in field settings (i.e. sediment supply, type of bar, vegetation established along channel), this experiment can still provide some insight into how peak flow and recession rate may shape bars. The primary influence of peak flow appears to be the volume and elevation of sediment deposition on the bar, with higher peaks depositing more material at higher elevations than lower peaks. This deposit can then impact local hydraulics for the remainder of the run, potentially steering additional sediment around the bar if it is large (Legleiter et al., 2011). For the bar examined here, a rapid recession rate resulted in emergence of the bar-top and scour along the edge, producing a small bar-top. A more gradual recession kept the bar submerged and deposition continued across the bar with minimal scour of the edge, resulting in a larger bar-top. In addition, more gradual recession rates were associated with less net sediment loss after peak flow. This is a particularly important consideration for regulated rivers where sediment supply is often limited and suggests that more gradual recession rates could better preserve a limited resource.

Restoration projects commonly include installing vegetation along or near banks for the purpose of providing stabilization to stream banks (Abernethy & Rutherfurd, 1998; Simon & Collinson, 2002) and to provide shade and reduce water temperature. Our results, along with those of Rominger et al. (2010) show that vegetation used in a sand bad channel may indeed retain sediment within the patch, but result in net scour due to enhanced erosion elsewhere in the channel. Further, a more rapid recession rate with vegetation on the bar resulted in significant scour of the downstream portion of the bar. These findings highlight the need for careful consideration of vegetation placement in restoration projects so as not to actually enhance scour or destabilize the channel. The formation of the cut-off chute in these experiments also demonstrates how vegetation might be used to increase channel complexity and diversity in habitat. In a natural channel, the chute would provide an area of refuge with shallower, slower moving water.

2.5. Conclusions

The responses of the bar documented in this study to different recession limb hydrographs suggests that point bars within sand bed systems are sensitive to both the peak flow and recession rate of unsteady flows. The primary impact of peak flow was the deposition of sand on the bar-top, with the higher peak flow depositing a larger volume of sand than the lower peak flow. One result of this was that the final bar-tops sat at a higher elevation in the channel for high peak runs compared to low peak runs. In addition, sediment deposited on the bar-top at peak would have changed local hydraulics for the remainder of the recession. For the high peak runs, the larger deposits could have caused flow and sediment to be diverted around the bar top, minimizing additional growth of the bar and resulting in the smaller, less distinct bar-tops. In contrast, less deposition during lower peaks did not divert flow and sediment around the bar-top, allowed continued deposition and bar growth through the remainder of the recession to produce large, more distinct bars.

Recession rate also influenced final bar forms, largely by bar-top emergence. The bar-tops of H10 and H10V may not have emerged because peak deposition was less than for high peak runs. However, the gradual recession rate kept the bar-tops of H10 and H10V sufficiently submerged for long enough to redistribute high flow deposits and prevent the bar-top from emerging or even coming close to emerging. As a result, sediment transport over the bar continued, resulting in a large, well-defined final bar form. In contrast, the bar-tops of H30, H30V, and H60 emerged during the recession. This was a combination of significant deposition during peak and rapid recession rates that did not provide sufficient time for redistribution of peak flow deposits to prevent the bar from emerging. Estimates of cross-sectional area for runs H10, H30, and H60 during a time-step with similar discharge show that emergence of the bar-top reduced cross-sectional area, likely increasing mean velocity. This drove greater scour in the thalweg and along bar edge, contributing to the smaller, less defined bar-top areas.

The main impacts of the dense vegetation patch installed on the bar for runs H10V and H30V were net scour, rather than net deposition seen in H10 and H30, and formation of the cut-off chute across the bar-top. While there was significant deposition within the vegetation patch itself, scour adjacent to the patch and in the thalweg was enhanced compared to runs without the vegetation. Despite net scour rather than deposition, the H10V bar was of similar size to H10, while H30V was larger than H30 though wider and shorter. Consistent with H10 and H30, the lower peak and more gradual recession of H10V resulted in a larger bar than the higher peak and faster recession of H30V. In addition, a cut-off chute formed across the bar-top in response to the vegetation. Sediment was conveyed through the chute, nearly refilling fully through the gradual recession of H10V, but not during the more rapid recession of H30V.

The varying responses of the bar provide some insight into the ways in which planned high flows on regulated systems might be designed to create the desired bar morphology to meet restoration goals. High flows require careful consideration, particularly where sediment supply is significantly reduced by impoundment in a reservoir. Peak flow magnitude can be used to influence the amount and elevation at which deposition occurs on the bar-top, and this deposit can have lasting impacts on local hydraulics and thus continued scour or deposition through the recession limb. The recession rate can influence the degree of redistribution and additional scour or deposition on the bar, and our results suggest that more gradual recession rates promote development of larger, well-defined bars than rapid recession rates. The use of vegetation in restoration requires careful consideration as well because in this experiment it resulted in net scour through the bar and pool. Vegetation may promote localized deposition, but increase scour elsewhere in the channel, potentially impacting overall channel stability.

While we studied a limited set of conditions, the results suggest that hydrograph form, in combination with additional factors like vegetation patches, do impact bar form. Further studies could provide additional insights into the influence of other factors we did not test. This includes hydrograph rising limbs, separately and in combination with a full hydrograph, and the response of gravel bed channels. In particular, further, understanding of bar response to hydrograph forms under a range of

sediment supply conditions would be especially useful for reaches downstream of dams where sediment is often in limited supply.

2.6. Works Cited

Abernethy, B., & Rutherfurd, I. D. (1998). Where along a river's length will vegetation most effectively stabilise stream banks? Geomorphology, 23(1), 55–75. https://doi.org/10.1016/S0169-555X(97)00089-5

Baker, D. W., Bledsoe, B. P., Albano, C. M., & Poff, N. L. (2011). Downstream effects of diversion dams on sediment and hydraulic conditions of Rocky Mountain streams. River Research and Applications, 27(3), 388–401. https://doi.org/10.1002/rra.1376

Bell, R. G., & Sutherland, A. J. (1983). Nonequilibrium Bedload Transport by Steady Flows. Journal of Hydraulic Engineering, 109(3), 351–367. https://doi.org/10.1061/(ASCE)0733-9429(1983)109:3(351)

Bombar, G., Elçi, Ş., Tayfur, G., Güney, M. Ş., & Bor, A. (2011). Experimental and Numerical Investigation of Bed-Load Transport under Unsteady Flows. Journal of Hydraulic Engineering, 137(10), 1276–1282. https://doi.org/10.1061/(ASCE)HY.1943-7900.0000412

Church, M. (1995). Geomorphic response to river flow regulation: Case studies and time-scales. Regulated Rivers: Research & Management, 11(1), 3–22. https://doi.org/10.1002/rrr.3450110103

Clark, G. M. (2010). Changes in Patterns of Streamflow From Unregulated Watersheds in Idaho, Western Wyoming, and Northern Nevada 1. JAWRA Journal of the American Water Resources Association, 46(3), 486–497. https://doi.org/10.1111/j.1752-1688.2009.00416.x

Dominick, D. S., & O'Neill, M. P. (1998). Effects of flow augmentation on stream channel morphology and riparian vegetation: Upper Arkansas River basin, Colorado. Wetlands, 18(4), 591–607. https://doi.org/10.1007/BF03161675

Dynesius, M., & Nilsson, C. (1994). Fragmanetaion and flow regulation of river systems in the northern third of the world. Science, 266, 753–762. https://doi.org/10.1126/science.266.5186.753

Ghimire, B., & Deng, Z. (2013). Event Flow Hydrograph–Based Method for Modeling Sediment Transport. Journal of Hydrologic Engineering, 18(8), 919–928. https://doi.org/10.1061/(ASCE)HE.1943-5584.0000710

Gordon, E., & Meentemeyer, R. K. (2006). Effects of dam operation and land use on stream channel morphology and riparian vegetation. Geomorphology, 82(3–4), 412–429. https://doi.org/10.1016/j.geomorph.2006.06.001

Griffiths, G. (1976). Transport of bedload by translation waves in an alluvial channel.

Hamlet, A. F., & Lettenmaier, D. P. (2007). Effects of 20th century warming and climate variability on flood risk in the western U.S. Water Resources Research, 43(6). https://doi.org/10.1029/2006WR005099

Hassan, M. A., Egozi, R., & Parker, G. (2006). Experiments on the effect of hydrograph characteristics on

vertical grain sorting in gravel bed rivers. Water Resources Research, 42(9). https://doi.org/10.1029/2005WR004707

Humphries, R., Venditti, J. G., Sklar, L. S., & Wooster, J. K. (2012). Experimental evidence for the effect of hydrographs on sediment pulse dynamics in gravel-bedded rivers. Water Resources Research, 48(1). https://doi.org/10.1029/2011WR010419

Kondolf, G. M. (1997). PROFILE: Hungry Water: Effects of Dams and Gravel Mining on River Channels. Environmental Management, 21(4), 533–551. https://doi.org/10.1007/s002679900048

Lake, P. S., Palmer, M. A., Liermann, C. A. R., Nilsson, C., Flörke, M., Alcamo, J., et al. (2012). Climate change and the world ' s river basins : anticipating management options. Wiley Online Library, (August 2015). https://doi.org/10.1890/060148

Lee, K. T., Liu, Y.-L., & Cheng, K.-H. (2004). Experimental investigation of bedload transport processes under unsteady flow conditions. Hydrological Processes, 18(13), 2439–2454. https://doi.org/10.1002/hyp.1473

Luce, C. H., & Holden, Z. A. (2009). Declining annual streamflow distributions in the Pacific Northwest United States, 1948–2006. Geophysical Research Letters, 36(16), L16401. https://doi.org/10.1029/2009GL039407

Magilligan, F. J., & Nislow, K. H. (2005). Changes in hydrologic regime by dams. Geomorphology, 71(1–2), 61–78. https://doi.org/10.1016/j.geomorph.2004.08.017

Mao, L. (2012). The effect of hydrographs on bed load transport and bed sediment spatial arrangement. Journal of Geophysical Research: Earth Surface, 117(F3), n/a-n/a. https://doi.org/10.1029/2012JF002428

Martin, R. L., & Jerolmack, D. J. (2013). Origin of hysteresis in bed form response to unsteady flows. Water Resources Research, 49(3), 1314–1333. https://doi.org/10.1002/wrcr.20093

Parker, G., Hassan, M., & Wilcock, P. (2007). 10 Adjustment of the bed surface size distribution of gravel-bed rivers in response to cycled hydrographs. Developments in Earth Surface Processes, 11, 241–285. https://doi.org/10.1016/S0928-2025(07)11127-5

Petts, G. E., & Gurnell, A. M. (2005). Dams and geomorphology: Research progress and future directions. Geomorphology, 71(1–2), 27–47. https://doi.org/DOI 10.1016/j.geomorph.2004.02.015

Phillips, C. B., Martin, R. L., & Jerolmack, D. J. (2013). Impulse framework for unsteady flows reveals superdiffusive bed load transport. Geophysical Research Letters, 40(7), 1328–1333. https://doi.org/10.1002/grl.50323

Poff, N. L., Olden, J. D., Merritt, D. M., & Pepin, D. M. (2007). Homogenization of regional river dynamics by dams and global biodiversity implications. Proceedings of the National Academy of Sciences, 104(14), 5732–5737. https://doi.org/10.1073/pnas.0609812104

Rominger, J. T., Lightbody, A. F., & Nepf, H. M. (2010). Effects of Added Vegetation on Sand Bar Stability and Stream Hydrodynamics. Journal of Hydraulic Engineering, 136(12), 994–1002. Retrieved from http://10.0.4.37/(ASCE)HY.1943-7900.0000215

Schnorbus, M., Werner, A., & Bennett, K. (2014). Impacts of climate change in three hydrologic regimes in British Columbia, Canada. Hydrological Processes, 28(3), 1170–1189. https://doi.org/10.1002/hyp.9661

Shen, Y., & Diplas, P. (2010). Modeling Unsteady Flow Characteristics of Hydropeaking Operations and Their Implications on Fish Habitat. Journal of Hydraulic Engineering, 136(12), 1053–1066. https://doi.org/10.1061/(ASCE)HY.1943-7900.0000112

Simon, A., & Collinson, A. J. C. (2002). Qunatifying th mechanical and hydrological effects of riparian vegetation on streambank stability. Earth Surface Processes and Landforms, 27(April), 527–546. https://doi.org/10.1002/esp.325

Singer, M. B. (2007). The influence of major dams on hydrology through the drainage network of the Sacramento River basin, California. River Research and Applications, 23(1), 55–72. https://doi.org/10.1002/rra.968

Viparelli, E., Gaeuman, D., Wilcock, P., & Parker, G. (2011). A model to predict the evolution of a gravel bed river under an imposed cyclic hydrograph and its application to the Trinity River. Water Resources Research, 47(2). https://doi.org/10.1029/2010WR009164

Waters, K. A., & Crowe Curran, J. (2016). Effects of an emergent vegetation patch on channel reach bathymetry and stability during repeated unsteady flows. Water Resources Research, 52(11), 9066–9085. https://doi.org/10.1002/2015WR018411

Waters, K. A., & Curran, J. C. (2015). Linking bed morphology changes of two sediment mixtures to sediment transport predictions in unsteady flows. Water Resources Research, 51(4), 2724–2741. https://doi.org/10.1002/2014WR016083

Wesche, T., Skinner, Q., Hasfurther, V., & Wolff, S. (1988). Stream channel response to flow depletion. Retrieved from http://library.wrds.uwyo.edu/wrp/88-19/88-19.pdf

Yao, H., & Georgakakos, A. (2001). Assessment of Folsom Lake response to historical and potential future climate scenarios: 2. Reservoir management. Journal of Hydrology, 249(1–4), 176–196. https://doi.org/10.1016/S0022-1694(01)00418-8

Yen, C., & Lee, K. T. (1995). Bed Topography and Sediment Sorting in Channel Bend with Unsteady Flow. Journal of Hydraulic Engineering, 121(8), 591–599. https://doi.org/10.1061/(ASCE)0733-9429(1995)121:8(591)

Young, W. J., & Davies, T. R. H. (1991). Bedload transport processes in a braided gravel-bed river model. Earth Surface Processes and Landforms, 16(6), 499–511. https://doi.org/10.1002/esp.3290160603

3.0. Hysteresis driven by armor loss and bed structure changes during unsteady flow

3.1. Introduction

Bedload hysteresis is a common phenomenon in which flux rates (q_s) vary for the same discharge on the rising and falling limbs of a hydrograph. Hysteresis can be clockwise (CW; greater q_s on the rising limb), counterclockwise (CCW; greater q_s on the falling limb), or more complex. Predicting q_s and total bedload flux (q_T) for an event is often complicated by hysteresis because q_s can vary so widely for a single discharge. However, the mechanisms behind bedload hysteresis often remain unclear. A better understanding of what drives hysteresis will not only improve predictions of q_s and q_T during hydrographs but will also provide basic information about mechanisms that increase or decrease q_s within the same channel.

In armored, gravel-bed channels, hysteresis may result from breakup of the coarser bed surface during high flow which exposes the finer grained sub-surface and increases q_s. However, this link remains tenuous because observing the bed at high flow is rarely possible, leading to ongoing uncertainty about what actually happens to armor structure. Instead, armor behavior is typically inferred from comparisons of the pre and post-event bed (e.g. Clayton & Pitlick, 2008; Vericat et al., 2006). Some studies have concluded that armor breaks up during high flow (Vericat et al., 2006), while others have concluded that it persists as a mobile feature of the bed (Andrews & Erman, 1986; Clayton & Pitlick, 2008; Gary Parker et al., 2007; Wilcock & DeTemple, 2005). Both findings may be correct, depending on whether the armor is static or mobile (e.g. Mao et al., 2011). Static armor forms with very limited sediment supply by winnowing of fine grains from the surface (Church et al., 1998; Hassan et al., 2006; G. Parker & Sutherland, 1990; Proffitt & Sutherland, 1983), resulting in a coarser, more structure and imbricated surface than mobile armor (Mao et al., 2011). As a result, static armor may persist through many high

flows, only breaking up and contributing to hysteresis during larger events. Mobile armor forms with a less limited sediment supply through near equal mobility of all grain sizes due to hiding effects (Parker & Klingeman, 1982; Proffitt & Sutherland, 1983). The coarse surface is maintained through exchange with the bedload and kinematic sorting of finer grains into the sub-surface (Gary Parker & Toro-Escobar, 2002; Wilcock, 2001). Mobile armor may also persist through high flows as a dynamic feature of the bed (Andrews & Erman, 1986; Clayton & Pitlick, 2008; Wilcock & DeTemple, 2005). Breakup, and contribution to hysteresis, occurs when there are insufficient coarse grains to replace those mobilized from the surface (Clayton & Pitlick, 2008; Dietrich W.E. et al., 1989; Gary Parker et al., 2007). However, whether mobile armor can also drive hysteresis before it fully breaks up remains uncertain. More certainty about armor dynamics during hydrographs is required to improve predictions of q_s and make definitive links to hysteresis.

There is evidence that hydrograph form itself influences armor persistence, and thus any resulting hysteresis. Most obviously, high flows can drive armor breakup (Orrú et al., 2006; Vericat et al., 2006). Rate of change may also be important, with more gradually changing hydrographs (snowmelt driven) promoting more armor development than "flashier" hydrographs (rain driven; Hassan et al., 2006). This could be the result of differences in durations at sub-critical τ. Gradual hydrographs typically have longer durations of sub-critical or lower τ than flashier events, which has been linked to more stable bed surface structure that could promote armor development or persistence (Haynes & Pender, 2007; Monteith & Pender, 2005; Ockelford & Haynes, 2013). Hydrograph rate of change can also alter τ actually applied to the bed. Shear stress can be significantly increased or decreased for a given discharge in an unsteady flow compared to the same discharge at steady-state conditions (Bombar et al., 2011; Ghimire & Deng, 2013; Shen & Diplas, 2010; Song & Graf, 1996). Predictions of q_s over the duration of floods could be greatly improved by knowing which hydrograph forms promote breakup and which promote persistence.

This flume-based study was designed to provide additional insight into drivers of hysteresis in an armored, gravel bed system. The first goal was to determine if hydrograph form impacted hysteresis. We

isolated the potential influences of hydrograph form by holding constant as many characteristics as possible among runs such as peak flow and estimated q_T, while varying only rate of change in discharge. Other potential drivers of hysteresis were controlled for, such as asymmetric hydrographs and changes in the sediment feed rate relative to transport capacity. We also sought to determine whether armor dynamics contributed to any observed hysteresis as is often hypothesized, and how this might have varied with hydrograph form. Additional runs investigated the impacts of a reduced sediment feed rate, hydrograph repetition, and a larger peak discharge.

3.2. Methods

3.2.1. Experiments

Flume experiments were run in the flume at the University of Idaho's Stream Lab at the Center for Ecohydraulics Research. The channel was 1 m wide with 15.3 m of mobile sediment and a 9.25 m test section. Flume slope was 0.009 but the slope of the sediment bed (S) was free to adjust. The bed fill and the sediment feed had a log-normal grain size distribution between 2-32 mm (D_{50} of 9 mm). Experiments were not scaled to a specific field site, but a general stream channel that the experiments would represent can be determined using geometric Froude scaling (Table 1; Graf, 1971; Mao, 2012; Gary Parker et al., 2003). Experimental runs consisted of four steady-state runs (SS) and seven hydrograph runs (HYD).

Table 1. Geometric Froude scaling of experiments.

	s (m/m)	*B (m)*	*minimum Q (m3/s)*	*peak Q (m3/s)*	*D50 (mm)*
flume	0.009	1	0.132	0.271	9.2
1/20 reduction factor	0.009	20	236	485	184
1/10 reduction factor	0.009	10	42	56	92

Conditioning runs at constant Q and feed rate (q_f) established similar beds before SS and HYD runs, and were run to dynamic equilibrium (S stabilized around 0.009 and q_s equal to q_f). The armor produced during conditioning runs was likely mobile, rather than static, because all grain sizes were mobile and we

supplied sediment, resulting in surface coarsening through kinematic sorting (G Parker & Klingeman, 1982; Wilcock, 2001). We started SS and HYD runs by slowly filling the flume from the downstream end with an auxiliary pump and the tailgate positioned high. Once the water level reached the estimated initial depth for the run we began the main flow from the upstream end, gradually increasing to the desired discharge while shutting off the auxiliary pump and adjusting the tailgate to obtain uniform flow.

SS runs were conducted prior to HYD runs so that the data collection could aid in the design of the hydrographs for HYD runs. The duration of SS runs varied (Table 2), but at minimum were long enough to collect at least four sets of data and exceed the duration we expected to run the given Q during hydrographs. SS runs helped to estimate the flow at which significant armor breakup would begin, which was the desired peak for HYD runs. In addition, the mean q_s for the SS runs was used to estimate q_T for HYD runs and determine durations for each time-step within HYD runs.

Table 2.

run	total duration (min)	peak Q (m^3/s)	sediment feed rate (kg/s)	total sediment feed (kg)	total estimated transport capacity[a] (kg)
SS158	278	0.158	0.014	239	239
SS196	127	0.196	0.022	168	168
SS233	213	0.233	0.033	426	426
SS271	108	0.271	0.045	293	293
HYD9	288	0.271	0.008 - 0.045	400	347
HYD43	300	0.271	0.008 - 0.045	398	347
HYD46	220	0.271	0.008 - 0.045	352	376
HYD9rf[b]	288	0.271	0 - 0.011	96	347
HYD46rf[b]	220	0.271	0 - 0.011	80	376

a. Estimated capacity for steady-state runs using Parker (1990). Estimated capacity for hydrographs based on average flux rates measure in steady-state runs.

b. rf indicates reduced feed run with the feed rate at 25% of the original.

HYD runs used four different using four shapes (Figure 1). Each shape was first run with the original q_f (HYD9, HYD43, HYD46, HYD60), then two were repeated with a 75% reduction in q_f (HYD9rf and HYD46rf). In addition, HYD46rpt was an immediate repetition of the same shape used in HYD46 without resetting the bed. Hydrographs were step-wise due to limitations of the pump system and

to all allow for data collection during single, discrete flows. At present, there is no single method for designing and scaling total duration or time-step duration (for stepped hydrographs) of experimental hydrographs (Lee et al., 2004). Previous experiments have generally chosen durations and shapes to suit best suit study goals (Bombar et al., 2011; Guney et al., 2013; Hassan et al., 2006; B. C. Phillips & Sutherland, 1990; Waters & Curran, 2015; Yen & Lee, 1995). For these experiments, total hydrograph duration was scaled to transport an estimated total of 350 ± 15 kg of bedload sediment (Table 2), based on the measured mean flux rates of the SS runs. This mass was chosen for practical reasons related to limitations of the sediment trap system, but also because it would be sufficient to scour approximately 80% of the bed surface to a depth of 16 mm, equivalent to the D_{50} of the initial bed surface. The mean q_s of SS runs was used to adjust the duration of individual time-steps to reach the desired total flux. The duration of peak flow, 30 min, was set to allow sufficient time for data collection and allow initiation of armor breakup.

The influence of hydrograph shape was isolated by keeping as many variables as possible constant between runs, including minimum discharge (Q_0), peak discharge (Q_p), and duration, total water volume, total sediment feed, and total estimated transport capacity (360 ± 15 kg, based on the mean q_s SS runs). Q_0 (0.132 m^3/s) produced minimal bedload which allowed data collection prior to significant bed adjustment. Q_p in three of the four hydrographs (0.271 m^3/s for 30 min) was scaled to initiate armor breakup. HYD60 used a higher Q_p (0.334 m^3/s) but shorter duration (22 min) to keep the estimated transport capacity of peak the same among all hydrographs. Experimental design also removed several potential drivers of hysteresis. Symmetrical hydrographs ensured hysteresis would not result from differences in the bedload transport capacity of the rising and falling limbs. In addition, q_f was held at a constant percentage of estimated q_s to minimize hysteresis driven by changes in the ratio of sediment supply to transport capacity.

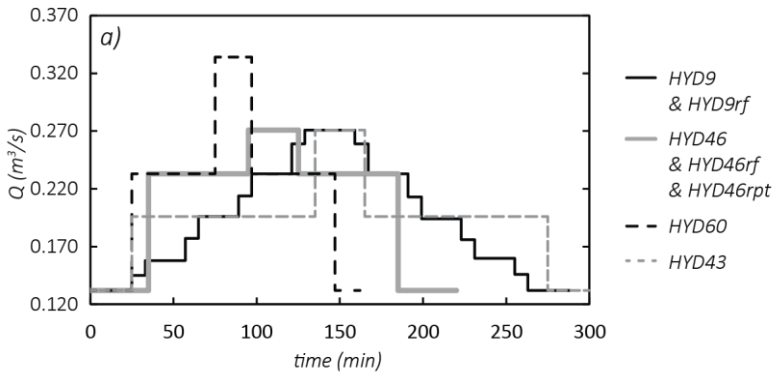

Figure 1. The four different hydrograph forms used in experiments.

The original and reduced q_F values were 12% and 3%, respectively, of the estimated flux rate based on the equation of Parker (1990) and the grain size distribution of the feed sediment. We chose to feed sediment below the estimated transport capacity because armored, gravel-bed rivers are often supply limited and these feed rates were selected after observing the flux for a variety of flows. This feed rate was selected by testing a range of feed rates and observing that they did not exceed the transport capacity, indicated by sediment accumulating where it was fed into the flume and increasing *S*. The range of discharges tested was approximately 0.177-0.233 m^3/s. However, for SS158, total sediment feed greatly exceeded total sediment flux, indicating that q_F was too high. However, we did not reduce q_F for flows $\leq$0.158 m^3/s during HYD runs. First, we wanted to keep q_F the same for SS and HYD runs for the purposes of comparing results (not discussed in this paper). Second, though q_F was too high, the total feed for discharges $\leq$0.158 m^3/s was only a small percentage of the total feed for the runs.

3.2.2. Data collection

Bedload flux was measured continuously through runs. Samples for bed surface grain size distributions and armor ratios were collected before (n = 4) and after runs (n = 5 to 7) in 20x20 cm areas in the test section, with the surface and sub-surface collected and analyzed separately. Pre-run samples were placed back into the bed before starting the run. Sonar scans consisted of 19 cross-sections, and were done 1-3 times per time-step (depending on time-step duration). We estimated loss of the original

armor surface, *A*, from the sonar scans by comparing elevation changes relative to the first sonar scan. The threshold for *A* was -20 mm, which was similar to the D_{90} of the original bed surface. We also estimated total armor loss, A_T, of a run by lightly spray-painting the original bed surface in three 1 m long sections and excavating them at the end of the run. Photos of the bed surface (taken through a clear sheet of plastic placed on the water surface) were taken after sonar scans within six cross-sections over the spray-painted areas. The resulting images were used to examine changes in the bed-surface grain size distribution through runs and the orientation of the longest axes of particles on the surface.

To estimate the bed surface grain size distribution for a given time-step, one photo was selected from selected from six cross-sections spread through the test section. Preference was given to photos closer to the middle of the channel to avoid effects of the flume walls, but image quality also dictated photo selection. Scale was determined for each photo from the scale bar placed within the image, then the images were cropped to an area 25x25 cm and overlain with a 2 cm grid. The b-axis of grains beneath grid vertices was determined as best as possible and measured. Grains were not counted twice if they sat under more than one intersection. This resulted in 752-832 grains measured per time-step. The resulting grain size distributions are not calibrated to samples taken from the bed but can be compared among themselves.

Photos were also used to examine the orientations of grain a-axes on the bed surface. For each time-step analyzed, three photos were selected from cross-sections spread through the test section. Again, preference was given to grains near the middle of the channel to avoid effects of the flume walls. Scale was determined, and images were cropped to 30x25 cm then overlain with a 5 cm grid. Rather than measure at grid vertices, we measured grains overlain by the horizontal lines, and only measured the angles for grains for which the a-axis was clearly discernible. This removed some uncertainty due to incorrectly identifying the a-axis. For each time-step, the angles of 321-364 grains were measured.

3.2.3. Modeling shear stress

The effects of the hydrographs on the variability in space and time in flow were analyzed using the one-dimensional unsteady shallow water or *Saint-Venant* equations. These set of equations describe

the conservation of mass and linear momentum in open-channel flow. In conservative form the system of partial differential equations is:

$$\frac{\partial W}{\partial t}+\frac{\partial F(W)}{\partial x}=G(W,x) \quad \text{Eq. 1}$$

where x and t are the space and time domain, respectively. The vector W and the functions F and G are defined according to:

$$W=\begin{pmatrix} A \\ Q \end{pmatrix} \quad \text{Eq. 2}$$

$$F=\begin{pmatrix} Q \\ \frac{Q^2}{A}+gI_1 \end{pmatrix} \quad \text{Eq. 3}$$

$$G=\begin{pmatrix} 0 \\ gI_2+gA\left(S_0-S_f\right) \end{pmatrix} \quad \text{Eq. 4}$$

where A is the wetted cross-sectional area, Q the discharge, S_0 and S_f the bed and energy slope, respectively, and g the acceleration due to the gravity. The terms I_1 and I_2 account for the hydrostatic pressure force and pressure forces induced by variations in longitudinal width. In our case, we simplified $I_2=0$ because the flume had a uniform width. Considering that our experiments were conducted in a 1 m wide channel equations 2 to 4 can be re-written as:

$$W=\begin{pmatrix} h \\ q \end{pmatrix} \quad \text{Eq. 5}$$

$$F = \begin{pmatrix} q \\ \frac{q^2}{h} + \frac{1}{2} g h^2 \end{pmatrix}$$ Eq. 6

$$G = \begin{pmatrix} 0 \\ gh\left(S_0 - S_f\right) \end{pmatrix}$$ Eq. 7

where h and q are the section-averaged flow depth and unit discharge, respectively. The system of equations is solved using the flux-difference-splitting scheme of Van Leer (1982). The local energy slope is estimated using the Manning's equation where the roughness coefficient can vary as a function of discharge and space. Once flow conditions (i.e. h and q) are obtained for a complete hydrograph we estimated the spatially distributed shear stress (τ) using:

$$\tau = \rho g R_h S_f$$ Eq. 8

where ρ is the water density and R_h is the hydraulics ratio. We explored the contribution of each term that controls τ by expanding Eq 8 using

$$\tau_u = \rho g R_h \left(S_0 - \frac{\partial h}{\partial x} - \frac{u}{g}\frac{\partial u}{\partial x} - \frac{1}{g}\frac{\partial u}{\partial t}\right)$$ Eq 9

where $u = q/h$ is the section-averaged flow velocity.

This model was used to investigate the impacts of unsteady flow during transitional periods between time-steps of hydrographs were for runs HYD9, HYD43, HYD46, and HYD60. Transitions were modeling using both the measured bed topography and a flat bed. First, the transitions were modeled using the measured centerline, which consisted of bed elevations from 19 cross-sections through the test-section. Because of the sparse data, the measured beds had abrupt transitions that were not realistic and

resulted in unrealistic spikes in estimated τ_u. Second, the transitions were modeled as a flat bed with the S measured for the time-step at the start of the transition. Because of the unrealistic results using the real bed topography, we relied on findings from the flat-bed cases.

3.3. Results

3.3.1. Drivers of hysteresis

The majority of hydrographs resulted in CCW hysteresis (Figure 2b), while HYD9 and HYD9rf resulted in figure-eight patterns (Figure 2a). Previous flume studies have also documented CCW hysteresis for an armored bed (e.g. Guney et al., 2013). To compare hysteresis among runs, we quantified the degree using the ratio $\frac{q_{pf}}{q_r}$, in which q_{pf} is the mean bedload flux rate of the peak and falling limb combined and q_r is the mean flux rate of the rising limb. We combined peak and falling limb data for two key reasons. First, some data collection, like sonar scans, occurred only once during peak. Second, we also noted that most rising limb bed responses were very similar (armor loss, flux rates, net deposition or scour), with significant differences generally beginning at peak and into the falling limbs.

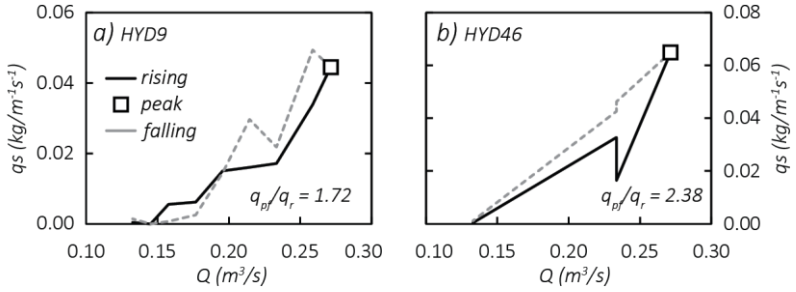

Figure 2. Examples of typical bedload hysteresis observed in HYD experiments. HYD9 and HYD9rf produced figure-eight hysteresis, with CW hysteresis for lower flows, and CCW hysteresis for higher flows. All other runs resulted in CCW hysteresis.

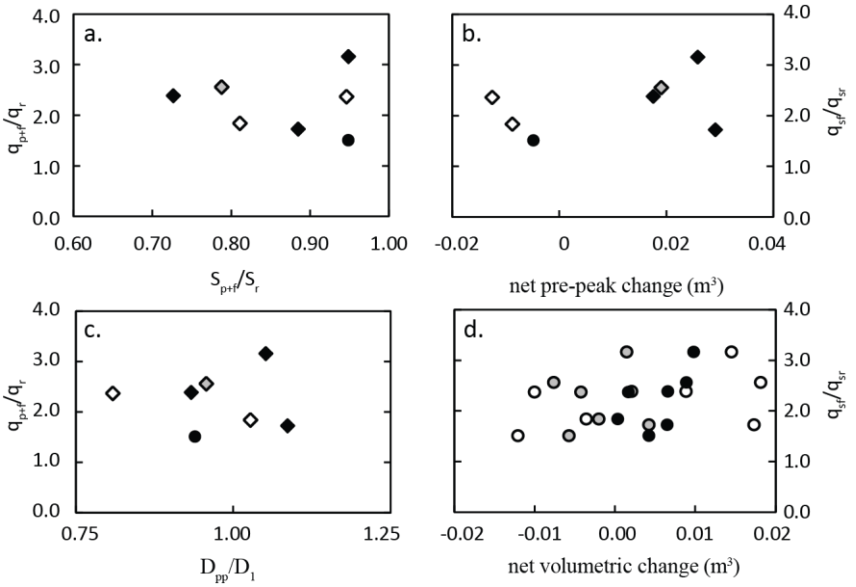

Figure 3. The observed bedload hysteresis, and the degree of hysteresis quantified as $\left(\frac{q_{pf}}{q_r}\right)$*, showed poor relationships with (a) changes in S from rising to falling limbs (b) net sediment deposition during rising limbs, (c) fining of the bed surface, or (d) net changes in fine (2-5.6 mm, black circles), medium (5.6-16 mm, white circles), or coarse (16-31.5 mm) grain size classes.*

We were able to rule out several potential drivers of the observed hysteresis patterns and degree of hysteresis $\left(\frac{q_{pf}}{q_r}\right)$, including bedforms, changes in *S*, sediment supply, and bed surface grain sizes. Bedforms could not explain hysteresis because they were never observed during experiments, nor were they visible in the sonar scans. Changes in *S* were also ruled out because CCW hysteresis would likely require steeper *S* during falling limbs, but the opposite was true for most runs. In addition, the relationship between the ratio of mean peak and falling limb slope to mean rising limb slope $\left(\frac{S_{pf}}{S_r}\right)$ and $\frac{q_{pf}}{q_r}$ is poor (Figure 3a). Incoming sediment supply could not have produced the CCW hysteresis because q_f was the same for a given flow on both limbs. Changes in sediment stored on the bed during the rising limb (total feed – total flux) also did not explain $\frac{q_{pf}}{q_r}$ (Figure 3b). We also considered changes in specific grain size classes (2-5.6, 5.6-16, and 16-31.5 mm) stored on the bed during the rising limb, estimating volumetric change using the known masses and grain size distributions of the sediment feed and samples of the

bedload flux. None of the three size classes appear to be driving $\frac{q_{pf}}{q_r}$ (Figure 3d). Further, repeat photos of the bed surface did not show significant changes in any size class or fining of the bed before peak (Figure 3c) in all but one run, HYD46rf (Kolmogorov-Smirnov test, α=0.05), which produced surface fining pre-peak. Overall, the relationship between changes in bed surface grain sizes and $\frac{q_{pf}}{q_r}$ is weak.

Modeling indicated that the unsteady flow during transitions did not have a significant impact on τ as flow increased or decreased. A comparison of mean τ_s and mean τ_u through the transitions shows that accounting for the unsteady components of τ results in, at the very most, a difference of about 2.5% (Figure 4). The magnitude and duration of this difference is likely within the uncertainty of the estimates of shear stress, and was not enough to significantly impact the bed surface structure or q_s.

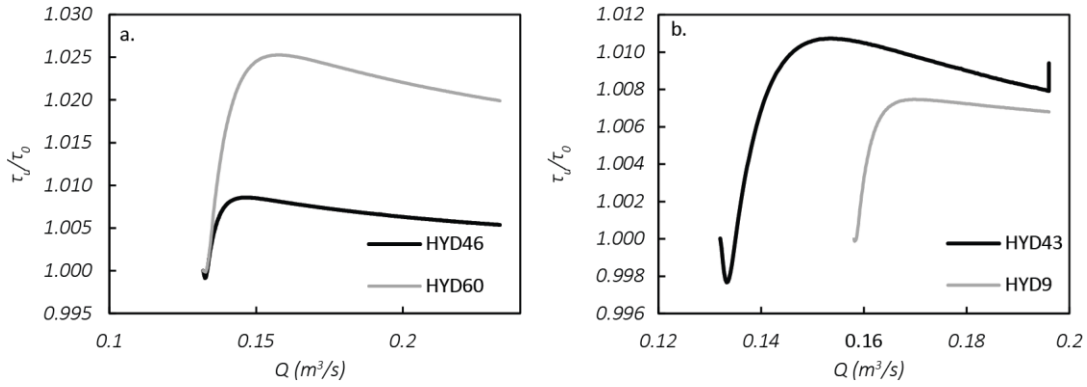

Figure 4. Two examples from modeling τ_u during transitions in flow. The ratio τ_u/τ_0 uses the mean values for the test-section.

The most likely driver of the observed hysteresis was *A*. Sonar derived estimates showed A_T was 3-24% of the bed area. Estimates of A_T from painted cross-sections were higher but relative losses among runs were consistent with sonar derived estimates, supporting use of repeat sonar scans to estimate *A*. There are several reasons why A_T estimates from sonar scans and those from the painted cross-sections are significantly. First, the threshold used to estimate armor loss from sonar scans was large, similar to the D90 of the original bed surface. This ensured we only included significant armor disruption, but also

likely excluded some losses. Further, armor disruption can be quickly obscured by new deposition which also suggests that sonar based estimates do not capture all losses. Third, it is likely that the sediment spray-painted on the bed surface was not all incorporated into the armor surface. Some portion was bedload that deposited when the preceding EQ run was stopped. If these grains could be excluded, it would lower estimates of A_T based on the painted areas.

For all runs, *A* was greater during the combined peak and falling limb than rising limb. To quantify the timing of *A* we used the ratio of peak and falling limb *A* relative to rising limb loss, $\frac{A_{pf}}{A_r}$, much like the ratio for hysteresis. When $\frac{q_{pf}}{q_r}$ is plotted as a function of $\frac{A_{pf}}{A_r}$, all runs collapse into a single relationship (Figure 5a). This indicates that regardless of peak flow or the sediment feed rate, greater *A* during peak and falling limbs resulted in increased q_s, producing CCW hysteresis. Further, *A* was not only driving hysteresis but how pronounced the hysteresis was as $\frac{q_{pf}}{q_r}$ increased with $\frac{A_{pf}}{A_r}$.

The relationship between $\frac{q_{pf}}{q_r}$ and $\frac{A_{pf}}{A_r}$ seen in Figure 5a does not result from plotting two different measures of bedload flux because *A* can be differentiated from scour. First, *A* required a minimum of -20 mm in elevation change, while any threshold for general scour should be much lower. Second, *A* was estimated relative to the original bed surface, while scour would be estimated relative to the surface of the previous time-step. Third, *A* could occur only once per location, but scour could occur repeatedly in the same place. As a result, it is possible to have significant scour for a given time-step, but minimal disturbance of the original armor. This becomes more evident when plotting all estimates of *A* as a function of scour for the same time-step (Figure 5c). We also plotted $\frac{q_{pf}}{q_r}$ as a function of peak and falling limb scour relative to rising limb scour ($\frac{\Delta e_{pf}}{\Delta e_r}$; Figure 5b). The threshold for scour was -5 mm, with Δe estimated relative to the bed of the previous time-step. The plot suggests some relationship between $\frac{\Delta e_{pf}}{\Delta e_r}$ and $\frac{q_{pf}}{q_r}$, but $\frac{A_{pf}}{A_r}$ still provides a stronger explanation for hysteresis.

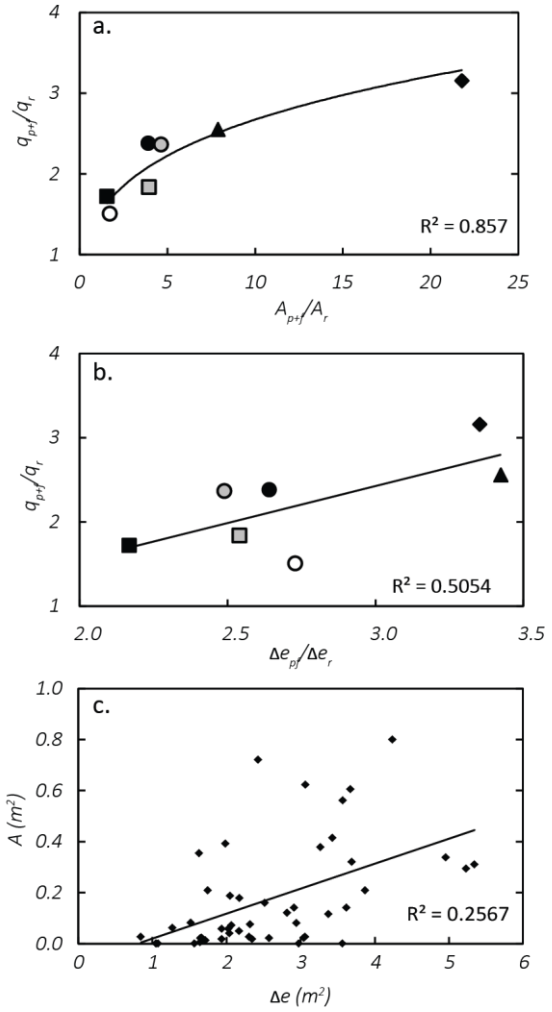

Figure 5. (a) Hysteresis, $\frac{q_{pf}}{q_r}$, plotted as a function of the ratio of peak and falling limb armor loss to rising limb armor loss, $\frac{A_{pf}}{A_r}$. The relationship provides strong evidence for armor loss as the driver of hysteresis. (b) Hysteresis, $\frac{q_{pf}}{q_r}$, plotted as a function of the ratio of peak and falling limb scour to rising limb scour, $\frac{\Delta e_{pf}}{\Delta e_r}$. (c) Estimated scour, Δe, plotted with the estimated armor loss, A, for all time-steps of HYD runs, indicating that significant scour does not always correspond with significant armor loss.

3.3.2. Drivers of armor loss

If *A* drove hysteresis, what drove differences in *A*? Similar to $\frac{q_{pf}}{q_r}$, we were able to rule out changes in *S*, bed surface grain size distributions, pre-peak volumetric change, and net change in specific

grain size fractions as drivers of $\frac{A_{pf}}{A_r}$ (Figure 6). However, results supported rising limb changes in bed surface structure as the driver of $\frac{A_{pf}}{A_r}$. We examined differences in rising limb bed structure indirectly because the coverage and resolution of sonar scans was insufficient to quantify bed structure. Indirect indicators of bed surface structure included porosity (inversely related to packing) and grain a-axis orientation.

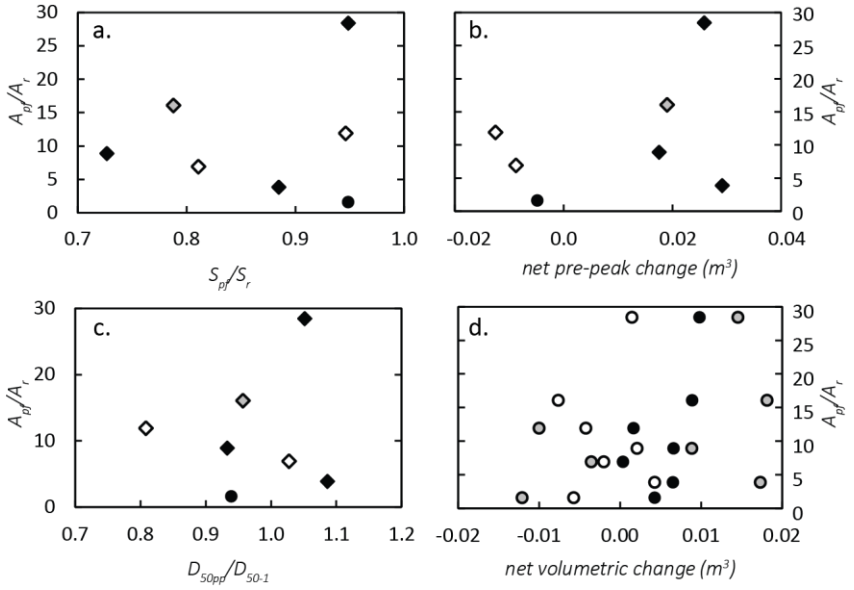

Figure 6. The differences in rising and falling limb armor losses, $\frac{A_{pf}}{A_r}$, were not driven by (a) changes in S from rising to falling limbs (b) net sediment deposition during rising limbs, (c) fining of the bed surface, or (d) net changes in fine (2-5.6 mm, black circles), medium (5.6-16 mm, white circles), or coarse (16-31.5 mm) grain size classes.

The pre-peak porosity of rising limb deposits, ϕ_{pp} (runs HYD9, HYD43, HYD46, and HYD60 only) was estimated using the mean elevation change from sonar scans and known mass of retained sediment. This assumes relatively uniform deposition over the bed, which was supported by sonar scans. The resulting estimates of ϕ_{pp} (0.49-0.67) are on the high end of field measurements for gravel deposits but still provide a proxy for comparison. Though we only have four runs to compare, higher ϕ_{pp} (lower

packing) was associated with greater A_{pf} (Figure 7a). In addition, greater ϕ_{pp} resulted in more pronounced CCW hysteresis (Figure 7a).

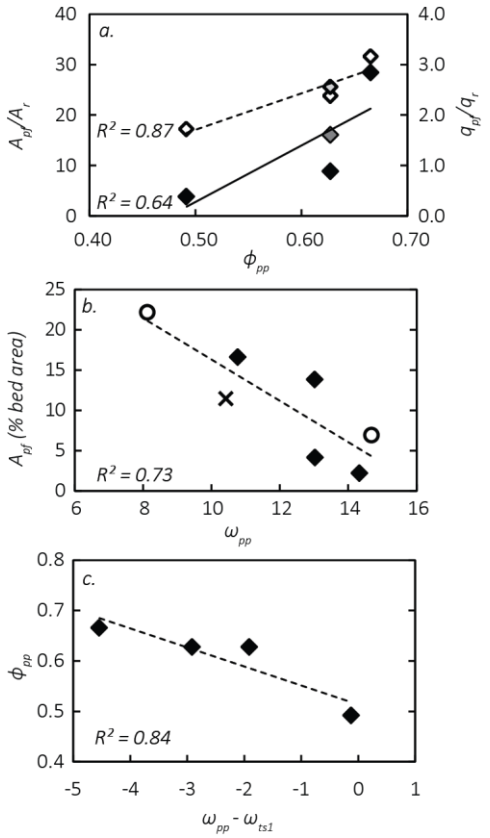

Figure 7. (a) Armor loss as $\frac{A_{pf}}{A_r}$ and hysteresis $\frac{q_{pf}}{q_r}$ plotted as a functions of the porosity of pre-peak deposition, ϕ_{pp}. Only four runs had net deposition prior to peak (HYD9, HYD43, HYD46, and HYD60). The black and dark gray diamonds (HYD60) are $\frac{A_{pf}}{A_r}$, and the white and light gray (HYD60) diamonds are $\frac{q_{pf}}{q_r}$. (b) Peak and falling limb armor loss, A_{pf}, as a function of the percentage of surface grains with a-axes aligned in the direction of the flow, ω_{pp}. Black diamonds are runs at the original feed rate, circles are runs at the reduced feed rate, and the x is the higher peak run, HYD60. (c) Pre-peak bed porosity, $\omega_{pp,}$ as a function of the change in grain a-axes aligned with the flow from the first time-step to just before peak (ω_{pp}- $\omega_{ts1)}$.

The orientation of grain a-axes can indicate the degree of bed surface organization, with flow parallel orientations indicative of more structured beds (Powell et al., 2016). In these experiments, we found that beds with more grains in flow parallel orientations (90±10°; see supplemental) just before peak

flow, ω_{pp}, were associated with less A_{pf} (Figure 7b). This suggests that beds with more ω_{pp} were indeed structured in a way that reduced sediment mobility. This is further supported by the increase of ω_{pp} with decreasing ϕ_{pp} (Figure 7c).

3.3.3. Impact of hydrograph form on bed structure

A variety of parameters have been previously used to quantify the unsteadiness of flows and predict sediment transport (Bombar et al., 2011; Lee et al., 2004; DE SUTTER et al., 2001). We tested the flow work parameter and unsteadiness parameters of Lee et al. (2004), De Sutter et al. (2001), Bombar et al. (2011), and Waters and Curran (2015) as predictors of changes in bed structure as seen in ϕ_{pp}, and ω_{pp}, but none performed satisfactorily. We tested additional, simper hydrograph characteristics such as mean rates of change in discharge, increase in flow to peak, and durations of low and high flows. The ratio between low and high flow durations of the rising limb, $\frac{Q_L}{Q_H}$, proved to be the best predictor of both ϕ_{pp}, and ω_{pp} (Figure 8). Q_L was ≤0.175 m^3/s because higher flows exceeded the estimated critical τ for the D_{84s} of the initial bed surface, and q_s increased significantly above 0.175 m^3/s in both SS and HYD runs. As $\frac{Q_L}{Q_H}$ increased, ϕ_{pp} decreased and ω_{pp} increased. This suggests that though the τ applied by Q_L did not significantly mobilize the bed, it resulted in smaller movements of grains that produced a more stable bed surface structure.

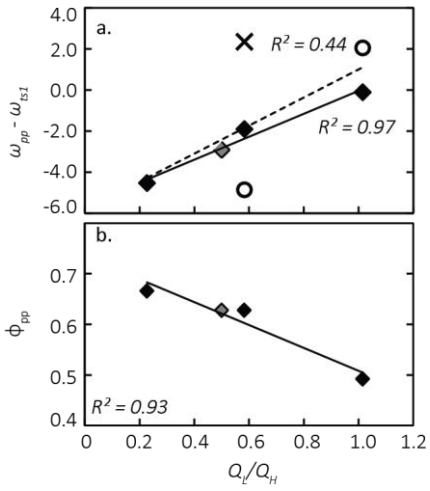

Figure 8. The ratio of rising limb low flow duration to high flow duration was a significant driver of bed structural changes. (a) change in grain a-axes aligned with the flow from the first time-step to just before peak (ω_{pp}- ω_{ts1}).

3.4. Discussion

3.4.1. Hysteresis driven by armor loss

Previous work has inferred that armor loss can drive bedload hysteresis (e.g. Kuhnle, 1992; Milhous & Klingeman, 1971) because exposure of the finer sub-surface increases q_s (Ashworth & Ferguson, 1989; Bathurst, 2007; Beschta, 1967; Emmett, 1976; Jackson & Beschta, 1982; R. T. Milhous, 1973; Ryan et al., 2002; Vericat et al., 2006). However, this inference is typically based on examination of armor after a hydrograph, with no knowledge of the timing of *A* and whether it coincided with increasing q_s. We are unaware of previous studies that have quantified *A* throughout a hydrograph. Doing so in this experiment allowed us to connect *A* to the observed hysteresis, showing that A_{pf} was greater than A_r as would be expected for CCW hysteresis (Figure 5a).

3.4.2. Stress history

The influence of antecedent flow or τ on a bed is often referred to as the stress history. Previous investigations of the stress history have shown that bed stability increases with the duration of low τ. On the grain scale, stabilization results from imbrication and flow parallel alignment of a-axes (Curran & Waters, 2014; Haynes & Pender, 2007; Ockelford & Haynes, 2013; Reid et al., 1985). On larger scales, prolonged low τ can produce vertical settlement and general consolidation (Ockelford & Haynes, 2013). While these previous findings are the result of single, steady flows, they still provide support for the observation in this study that longer Q_L duration relative to Q_H during rising limbs resulted in greater packing (lower porosity; Figure 8b) and increased grain stability (a-axis alignments; Figure 8a).

Less is known about the impacts of changing τ during unsteady flows on bed surface structure, and if the effects vary with hydrograph form. Our findings suggest that for armored, gravel bed streams, pre-peak bed stability increases with $\frac{Q_L}{Q_H}$, which then determines the degree of *A* initiated by peak flow. Previous flume experiments have also noted the influence of hydrograph form on bed structure. Hassan et al. (2006) found that more gradually changing hydrograph forms promoted armor development more than "flashier" hydrographs. Similarly, Mao (2012) documented greater packing and smoother bed surfaces

following gradual hydrographs than after more quickly changing flows. However, the impacts of peak flow cannot be ruled out for these two experiments because both Mao (2012) and Hassan et al. (2006) varied peak flow magnitude and duration among hydrographs. Our findings indicate that hydrograph form is indeed an important influence of bed surface structure because all runs had the same magnitude and duration of peak (with the exception of HYD60).

Hydrograph driven changes to bed structure can subsequently influence resulting bedload hysteresis. For the conditions of this experiment, as $\frac{Q_L}{Q_H}$ decreased, so did bed stability, driving more pronounced CCW hysteresis (Figure 5a). Mao (2012) also linked bed structure changes to hysteresis, but in contrast to this experiment, observed CW hysteresis resulting from greater falling limb bed stability. These seemingly opposing findings might be explained by numerous differences between experiments (grain size distributions, shear stresses relative to critical etc.). However, similar work (Guney et al., 2013; Waters & Curran, 2015) suggests that differences in initial bed conditions are the most likely driver of opposing hysteresis patterns. For this study, beds were conditioned by a steady flow run to equilibrium. In contrast, Mao (2012) applied a steady flow for a set duration of four hours, which may have resulted in a comparatively less structured, stable bed surface and greater transport on rising limbs. This is supported by Waters and Curran (2015), who observed CCW or figure-eight hysteresis during hydrographs that followed steady flows run to dynamic equilibrium, but CW hysteresis for repeated hydrographs. Similarly, Guney et al. (2013) found that antecedent flows that armored the bed resulted in CCW hysteresis but antecedent flows that did armor the bed resulted in CW hysteresis.

This and previous studies indicate that improving predictions of q_s during hydrographs will require consideration of the impacts of both antecedent conditions and hydrograph form. Two studies have incorporated hydrograph form by using separate reference shear stresses, τ_r, for the rising and falling limbs of hydrographs (Mao, 2012; Water and Curran, 2015). Both studies found generally higher τ_r during falling than rising limbs, driving CW hysteresis in most cases. In contrast, the CCW hysteresis

we observed suggests that τ_r would likely be greater during rising limbs for this experiment. This discrepancy may be explained by differences in initial bed stability (i.e. degree of armoring, particle orientation), highlighting the need to better understand and quantify how the state of the bed surface at the start of a hydrograph impacts the direction of change in stability.

3.4.3. Applications to hydropower

Our findings regarding the impacts of hydrograph form on bedload structure (especially armor breakup) and resulting q_s and hysteresis direction have a range of potential applications for hydropower. In particular, this includes informing the design of controlled floods for the desired impact on the bed surface downstream. Alteration of the natural flow regime by dam operations, combined with a reduction in incoming sediment supply, has degraded instream habitat downstream of many hydropower dams. In gravel-bed channels, this often includes significant coarsening and armoring of the bed, impacting the availability of habitat for macroinvertibrates (e.g. Gibbins et al., 2007), spawning fish (e.g. Kondolf, 2000) and even vegetation (e.g. Mahoney & Rood, 1998; Rood et al., 1995). Habitat mitigation is required in the relicensing of hydropower facilities through the Federal Energy Regulatory Commission (FERC), and increasingly this has included designing "floods" mimic key characteristics of the pre-regulation hydrograph. Examples include (1) the addition of augmentation gravels combined with spring releases to improve channel conditions for spawning fish on the Trinity River, CA and (2) the high-flow experiments on the Colorado River through the Grand Canyon aimed at restoring sand bars. Our study, along with others (e.g. Hassan et al., 2006; Waters and Curran, 2015; Mao, 2012), suggest that hydrographs can be designed to either increase or decrease bed surface stability, which in turn increases or decreases q_s, in order to aid in meeting restoration goals. Further, as hydrographs on both regulated and unregulated systems shift in response to climate change, our findings about the influence of hydrograph form on bedload transport processes provide insight into expected impacts. Our findings suggest that shifts to less gradually changing hydrographs may decrease bed stability. Downstream of dams this could impact habitat availability through changes in bed grain size distributions and scour. For unregulated

channels entering reservoirs, greater bedload sediment influxes could impact the lifespan of hydropower facilities.

3.5. Conclusions

Two primary findings can be drawn from this flume-based investigation of hysteresis during different hydrographs in an armored, gravel bed channel. First, we used repeat sonar scans to estimate armor loss throughout hydrographs, demonstrating that armor losses were a primary driver of hysteresis in bedload flux. This mechanism for hysteresis has long been hypothesized, but not previously documented directly. All runs had CCW or figure-eight (CCW at higher flows) hysteresis patterns, but the degree of hysteresis, quantified as $\frac{q_{pf}}{q_r}$, increased as peak and falling limb armor losses were greater relative to rising limb losses, $\frac{A_{pf}}{A_r}$.

The second main finding was that the amount of armor loss during peak and falling limbs was the result of bed structure and stability at the end of the rising limb, which was driven largely by hydrograph form. Hydrographs with longer low flow durations before peak resulted in greater bed surface stability than hydrographs with less time at low flow prior to peak. Bed surface structure was inferred indirectly by estimating the porosity (tighter packing) of pre-peak deposition and changes in the percentage of surface grains with their a-axes aligned with the flow direction. More stable beds prior to peak flow (lower porosity and more grains with a-axes aligned with the flow) resulted in less armor loss during peak and falling limbs than less stable beds.

3.6. References Cited

Andrews, E. D., & Erman, D. C. (1986). Persistence in the Size Distribution of Surficial Bed Material During an Extreme Snowmelt Flood. Water Resources Research, 22(2), 191–197. https://doi.org/10.1029/WR022i002p00191

Ashworth, P. J., & Ferguson, R. I. (1989). Size-selective entrainment of bed load in gravel bed streams. Water Resources Research, 25(4), 627–634. https://doi.org/10.1029/WR025i004p00627

Bathurst, J. C. (2007). Effect of Coarse Surface Layer on Bed-Load Transport. Journal of Hydraulic

Engineering, 133(11), 1192–1205. https://doi.org/10.1061/(ASCE)0733-9429(2007)133:11(1192)

Beschta, R. (1967). Conceptual models of sediment transport in streams. Retrieved from http://www.sidalc.net/cgi-bin/wxis.exe/?IsisScript=COLPOS.xis&method=post&formato=2&cantidad=1&expresion=mfn=024789

Bombar, G., Elçi, Ş., Tayfur, G., Güney, M. Ş., & Bor, A. (2011). Experimental and Numerical Investigation of Bed-Load Transport under Unsteady Flows. Journal of Hydraulic Engineering, 137(10), 1276–1282. https://doi.org/10.1061/(ASCE)HY.1943-7900.0000412

Church, M., Hassan, M. A., & Wolcott, J. F. (1998). Stabilizing self-organized structures in gravel-bed stream channels: Field and experimental observations. Water Resources Research, 34(11), 3169–3179. https://doi.org/10.1029/98WR00484

Clayton, J. A., & Pitlick, J. (2008). Persistence of the surface texture of a gravel-bed river during a large flood. Earth Surface Processes and Landforms, 33(5), 661–673. https://doi.org/10.1002/esp.1567

Curran, J. C., & Waters, K. A. (2014). The importance of bed sediment sand content for the structure of a static armor layer in a gravel bed river. Journal of Geophysical Research: Earth Surface, 119(7), 1484–1497. https://doi.org/10.1002/2014JF003143

Dietrich W.E., Kichner J.W., Ikeda H., & Iseya F. (1989). Sediment Supply and the Development of the Surface Layer in Gravel Bedded Rivers. Nature, 340, 215–217. Retrieved from https://www.nature.com/articles/340215a0

Emmett, W. (1976). Bedload transport in two large, gravel-bed rivers, Idaho and Washington.

Ghimire, B., & Deng, Z. (2013). Event Flow Hydrograph–Based Method for Modeling Sediment Transport. Journal of Hydrologic Engineering, 18(8), 919–928. https://doi.org/10.1061/(ASCE)HE.1943-5584.0000710

Gibbins, C., Vericat, D., Batalla, R. J., & Gomez, C. M. (2007). Shaking and moving: low rates of sediment transport trigger mass drift of stream invertebrates. Canadian Journal of Fisheries and Aquatic Sciences, 64(1), 1–5. https://doi.org/10.1139/f06-181

Graf, W. H. (1971). Hydraulics of Sediment Transport. New York: McGraw Hill.

Guney, M. S., Bombar, G., & Aksoy, A. O. (2013). Experimental Study of the Coarse Surface Development Effect on the Bimodal Bed-Load Transport under Unsteady Flow Conditions. Journal of Hydraulic Engineering, 139(1), 12–21. https://doi.org/10.1061/(ASCE)HY.1943-7900.0000640

Hassan, M. A., Egozi, R., & Parker, G. (2006). Experiments on the effect of hydrograph characteristics on vertical grain sorting in gravel bed rivers. Water Resources Research, 42(9). https://doi.org/10.1029/2005WR004707

Haynes, H., & Pender, G. (2007). Stress History Effects on Graded Bed Stability. Journal of Hydraulic Engineering, 133(4), 343–349. https://doi.org/10.1061/(ASCE)0733-9429(2007)133:4(343)

Jackson, W. L., & Beschta, R. L. (1982). A model of two-phase bedload transport in an oregon coast range stream. Earth Surface Processes and Landforms, 7(6), 517–527. https://doi.org/10.1002/esp.3290070602

Kondolf, G. M. (2000). Assessing Salmonid Spawning Gravel Quality. Transactions of the American

Fisheries Society, 129(1), 262–281. https://doi.org/10.1577/1548-8659(2000)129<0262:ASSGQ>2.0.CO;2

Kuhnle, R. A. (1992). Bed load transport during rising and falling stages on two small streams. Earth Surface Processes and Landforms, 17(2), 191–197. https://doi.org/10.1002/esp.3290170206

Lee, K. T., Liu, Y.-L., & Cheng, K.-H. (2004). Experimental investigation of bedload transport processes under unsteady flow conditions. Hydrological Processes, 18(13), 2439–2454. https://doi.org/10.1002/hyp.1473

Mahoney, J. M., & Rood, S. B. (1998). Streamflow requirements for cottonwood seedling recruitment—An integrative model. Wetlands, 18(4), 634–645. https://doi.org/10.1007/BF03161678

Mao, L. (2012). The effect of hydrographs on bed load transport and bed sediment spatial arrangement. Journal of Geophysical Research: Earth Surface, 117(F3), n/a-n/a. https://doi.org/10.1029/2012JF002428

Mao, L., Cooper, J. R., & Frostick, L. E. (2011). Grain size and topographical differences between static and mobile armour layers. Earth Surface Processes and Landforms, 36(10), 1321–1334. https://doi.org/10.1002/esp.2156

Milhous, R., & Klingeman, P. (1971). Bed-Load Transport in Mountain Streams.

Milhous, R. T. (1973, May 3). Sediment transport in a gravel-bottomed stream. Retrieved from https://ir.library.oregonstate.edu/concern/graduate_thesis_or_dissertations/bv73c272r?locale=en

Monteith, H., & Pender, G. (2005). Flume investigations into the influence of shear stress history on a graded sediment bed. Water Resources Research, 41(12). https://doi.org/10.1029/2005WR004297

Ockelford, A.-M., & Haynes, H. (2013). The impact of stress history on bed structure. Earth Surface Processes and Landforms, 38(7), 717–727. https://doi.org/10.1002/esp.3348

Orrú, C., Blom, A., & Uijttewaal, W. S. J. (2006). Armor breakup and reformation in a degradational laboratory experiment: detailed measurements of spatial and temporal changes of the bed surface texture. Earth Surface Dynamics. https://doi.org/10.5194/esurf-2016-1

Parker, G., & Klingeman, P. (1982). 1982: On why gravel bed streams are paved. Water Resources Research 18, 1409-23. Retrieved from https://scholar.google.com/scholar?q=On+why+gravel+bed+streams+are+paved+water+resources&hl=en&as_sdt=0%2C13&as_ylo=1982&as_yhi=1982

Parker, G., & Sutherland, A. J. (1990). Fluvial armor. Journal of Hydraulic Research, 28(5), 529–544. https://doi.org/10.1080/00221689009499044

Parker, G., & Toro-Escobar, C. M. (2002). Equal mobility of gravel in streams: The remains of the day. Water Resources Research, 38(11), 46-1-46–8. https://doi.org/10.1029/2001WR000669

Parker, G., Toro-Escobar, C. M., Ramey, M., & Beck, S. (2003). Effect of Floodwater Extraction on Mountain Stream Morphology. Journal of Hydraulic Engineering, 129(11), 885–895. https://doi.org/10.1061/(ASCE)0733-9429(2003)129:11(885)

Parker, G., Hassan, M., & Wilcock, P. (2007). 10 Adjustment of the bed surface size distribution of gravel-bed rivers in response to cycled hydrographs. Developments in Earth Surface Processes, 11, 241–285. https://doi.org/10.1016/S0928-2025(07)11127-5

Phillips, B. C., & Sutherland, A. J. (1990). Temporal lag effect in bed load sediment transport. Journal of Hydraulic Research, 28(1), 5–23. https://doi.org/10.1080/00221689009499144

Proffitt, G. T., & Sutherland, A. J. (1983). TRANSPORT OF NON-UNIFORM SEDIMENTS. Journal of Hydraulic Research, 21(1), 33–43. https://doi.org/10.1080/00221688309499448

Reid, I., Frostick, L. E., & Layman, J. T. (1985). The incidence and nature of bedload transport during flood flows in coarse-grained alluvial channels. Earth Surface Processes and Landforms, 10(1), 33–44. https://doi.org/10.1002/esp.3290100107

Rood, S. B., Mahoney, J. M., Reid, D. E., & Zilm, L. (1995). Instream flows and the decline of riparian cottonwoods along the St. Mary River, Alberta. Canadian Journal of Botany, 73(8), 1250–1260. https://doi.org/10.1139/b95-136

Ryan, S. E., Porth, L. S., & Troendle, C. A. (2002). Defining phases of bedload transport using piecewise regression. Earth Surface Processes and Landforms, 27(9), 971–990. https://doi.org/10.1002/esp.387

Shen, Y., & Diplas, P. (2010). Modeling Unsteady Flow Characteristics of Hydropeaking Operations and Their Implications on Fish Habitat. Journal of Hydraulic Engineering, 136(12), 1053–1066. https://doi.org/10.1061/(ASCE)HY.1943-7900.0000112

Song, T., & Graf, W. H. (1996). Velocity and Turbulence Distribution in Unsteady Open-Channel Flows. Journal of Hydraulic Engineering, 122(3), 141–154. https://doi.org/10.1061/(ASCE)0733-9429(1996)122:3(141)

DE SUTTER, R., VERHOEVEN, R., & KREIN, A. (2001). Simulation of sediment transport during flood events: laboratory work and field experiments. Hydrological Sciences Journal, 46(4), 599–610. https://doi.org/10.1080/02626660109492853

Vericat, D., Batalla, R. J., & Garcia, C. (2006). Breakup and reestablishment of the armour layer in a large gravel-bed river below dams: The lower Ebro. Geomorphology, 76(1–2), 122–136. https://doi.org/10.1016/j.geomorph.2005.10.005

Waters, K. A., & Curran, J. C. (2015). Linking bed morphology changes of two sediment mixtures to sediment transport predictions in unsteady flows. Water Resources Research, 51(4), 2724–2741. https://doi.org/10.1002/2014WR016083

Wilcock, P. R. (2001). Toward a practical method for estimating sediment-transport rates in gravel-bed rivers. Earth Surface Processes and Landforms, 26(13), 1395–1408. https://doi.org/10.1002/esp.301

Wilcock, P. R., & DeTemple, B. T. (2005). Persistence of armor layers in gravel-bed streams. Geophysical Research Letters, 32(8), 1–4. https://doi.org/10.1029/2004GL021772

Yen, C., & Lee, K. T. (1995). Bed Topography and Sediment Sorting in Channel Bend with Unsteady Flow. Journal of Hydraulic Engineering, 121(8), 591–599. https://doi.org/10.1061/(ASCE)0733-9429(1995)121:8(591)